Deformed relativistic Hartree-Bogoliubov theory in continuum with a point-coupling functional: Examples of even-even Nd isotopes

Kaiyuan Zhang (张开元),[1] Myung-Ki Cheoun,[2] Yong-Beom Choi,[3] Pooi Seong Chong,[4] Jianmin Dong (董建敏),[5,6] Lisheng Geng (耿立升),[7] Eunja Ha,[2] Xiaotao He (贺晓涛),[8] Chan Heo,[4] Meng Chit Ho,[4] Eun Jin In,[9] Seonghyun Kim,[2] Youngman Kim,[10] Chang-Hwan Lee,[3] Jenny Lee,[4] Zhipan Li (李志攀),[11] Tianpeng Luo (骆天鹏),[1] Jie Meng (孟杰) ⊙,[1,*] Myeong-Hwan Mun,[12] Zhongming Niu (牛中明),[13,14] Cong Pan (潘琮),[1] Panagiota Papakonstantinou,[15] Xinle Shang (尚新乐),[5,6] Caiwan Shen (沈彩万),[16] Guofang Shen (申国防),[7] Wei Sun (孙玮),[11] Xiang-Xiang Sun (孙向向),[17,18] Chi Kin Tam,[4] Thaivayongnou ,[7] Chen Wang (王晨),[8] Sau Hei Wong,[4] Xuewei Xia (夏学伟),[19] Yijun Yan (晏一珺),[5,6] Ryan Wai-Yen Yeung,[4] To Chung Yiu,[4] Shuangquan Zhang (张双全),[1] Wei Zhang (张炜),[20] and Shan-Gui Zhou (周善贵)[17,18,21,22]

(DRHBc Mass Table Collaboration)

[1]*State Key Laboratory of Nuclear Physics and Technology, School of Physics, Peking University, Beijing 100871, China*
[2]*Department of Physics and Origin of Matter and Evolution of Galaxy (OMEG) Institute, Soongsil University, Seoul 156-743, Korea*
[3]*Department of Physics, Pusan National University, Busan 46241, Korea*
[4]*Department of Physics, The University of Hong Kong, Pokfulam 999077, Hong Kong*
[5]*Institute of Modern Physics, Chinese Academy of Sciences, Lanzhou 730000, China*
[6]*School of Physics, University of Chinese Academy of Sciences, Beijing 100049, China*
[7]*School of Physics, Beihang University, Beijing 102206, China*
[8]*College of Materials Science and Technology, Nanjing University of Aeronautics and Astronautics, Nanjing 210016, China*
[9]*Department of Energy Science, Sungkyunkwan University, Suwon 16419, Korea*
[10]*Rare Isotope Science Project, Institute for Basic Science, Daejeon 305-811, Korea*
[11]*School of Physical Science and Technology, Southwest University, Chongqing 400715, China*
[12]*Korea Institute of Science and Technology Information, Daejeon 34141, Korea*
[13]*School of Physics and Materials Science, Anhui University, Hefei 230601, China*
[14]*Institute of Physical Science and Information Technology, Anhui University, Hefei 230601, China*
[15]*Institute for Basic Science, Rare Isotope Science Project, Daejeon 34000, South Korea*
[16]*School of Science, Huzhou University, Huzhou 313000, China*
[17]*CAS Key Laboratory of Theoretical Physics, Institute of Theoretical Physics, Chinese Academy of Sciences, Beijing 100190, China*
[18]*School of Physical Sciences, University of Chinese Academy of Sciences, Beijing 100049, China*
[19]*School of Physics and Electronic Engineering, Center for Computational Sciences, Sichuan Normal University, Chengdu 610068, China*
[20]*School of Physics and Microelectronics, Zhengzhou University, Zhengzhou 450001, China*
[21]*Center of Theoretical Nuclear Physics, National Laboratory of Heavy Ion Accelerator, Lanzhou 730000, China*
[22]*Synergetic Innovation Center for Quantum Effects and Application, Hunan Normal University, Changsha 410081, China*

Background: The study of exotic nuclei far from the β stability line is stimulated by the development of radioactive ion beam facilities worldwide and brings opportunities and challenges to existing nuclear theories. Including self-consistently the nuclear superfluidity, deformation, and continuum effects, the deformed relativistic Hartree-Bogoliubov theory in continuum (DRHBc) has turned out to be successful in describing both stable and exotic nuclei. Due to several challenges, however, the DRHBc theory has only been applied to study light nuclei so far.

Purpose: The aim of this work is to develop the DRHBc theory based on the point-coupling density functional and examine its possible application for all even-even nuclei in the nuclear chart by taking Nd isotopes as examples.

Method: The nuclear superfluidity is taken into account via Bogoliubov transformation. Densities and potentials are expanded in terms of Legendre polynomials to include the axial deformation degrees of freedom. Sophisticated relativistic Hartree-Bogoliubov equations in coordinate space are solved in a Dirac Woods-Saxon basis to consider the continuum effects.

Results: Numerical convergence for energy cutoff, angular momentum cutoff, Legendre expansion, pairing strength, and (un)constrained calculations are confirmed for the DRHBc theory from light nuclei to heavy nuclei. The ground-state properties of even-even Nd isotopes are calculated with the successful density functional PC-

PK1 and compared with the spherical nuclear mass table based on the relativistic continuum Hartree-Bogoliubov (RCHB) theory as well as the available data. The calculated binding energies are in very good agreement with the existing experimental values with a rms deviation of 0.958 MeV, which is remarkably smaller than 8.301 MeV in the spherical case. The predicted proton and neutron drip-line nuclei for Nd isotopes are respectively ^{120}Nd and ^{214}Nd, in contrast with ^{126}Nd and ^{228}Nd in the RCHB theory. The experimental quadrupole deformations and charge radii are reproduced well. An interesting decoupling between the oblate shape $\beta_2 = -0.273$ contributed by bound states and the nearly spherical one $\beta_2 = 0.047$ contributed by continuum is found in ^{214}Nd. Contributions of different single-particle states to the total neutron density are investigated and an exotic neutron skin phenomenon is suggested for ^{214}Nd. The proton radioactivity beyond the proton drip line is discussed and ^{114}Nd, ^{116}Nd, and ^{118}Nd are predicted to be candidates for two-proton or even multiproton radioactivity.

Conclusions: The DRHBc theory based on the point-coupling density functional is developed and detailed numerical checks are performed. The techniques to construct the DRHBc mass table for even-even nuclei are explored and extended for all even-even nuclei in the nuclear chart by taking Nd isotopes as examples. The available experimental data are reproduced well. The deformation and continuum effects on drip-line nuclei, exotic neutron skin, and proton radioactivity are presented.

I. INTRODUCTION

In nuclear physics, the study of the properties of exotic nuclei—nuclei with extreme numbers of protons or neutrons—is one of the top priorities, as it can lead to new insights into the origins of the chemical elements in stars and star explosions [1]. Although radioactive ion beams (RIBs) have extended our knowledge of nuclear physics from stable nuclei to exotic ones far away from the valley of stability, it is still a goal to reach the neutron drip line up to mass number $A \approx 100$ with the new generation of RIB facilities developed around the world, including the Cooler Storage Ring (CSR) at the Heavy Ion Research Facility in Lanzhou (HIRFL) in China [2], the RIKEN Radioactive Ion Beam Factory (RIBF) in Japan [3], the Rare Isotope Science Project (RISP) in Korea [4], the Facility for Antiproton and Ion Research (FAIR) in Germany [5], the Second Generation System On-Line Production of Radioactive Ions (SPIRAL2) at GANIL in France [6], the Facility for Rare Isotope Beams (FRIB) in the USA [7], etc.

The nuclear mass or binding energy is of crucial importance not only in nuclear physics, but also in other fields, such as astrophysics [8,9]. It has been always a priority in nuclear physics to explore the limit of nuclear binding [10–12]. Experimentally, the existence of about 3200 nuclides has been confirmed [13] and the masses of about 2500 nuclides have been measured [14,15]. The proton drip line has been determined up to neptunium [16], but the neutron drip line is known only up to neon [13]. In the foreseeable future, most neutron-rich nuclei far from the valley of stability will remain beyond the experimental capability. Therefore, it is urgent to develop a theoretical nuclear mass table with predictive power to have a complete understanding of the nature of such nuclei.

Theoretically, a lot of efforts have been made to predict nuclear masses and to explore the great unknowns of the nuclear landscape [10,12,17–35]. Precise descriptions of nuclear masses have been achieved with various macroscopic-microscopic models [17–20]. Several Skyrme [10,21–24] or Gogny [25–27] Hartree-Fock-Bogoliubov mass-table-type calculations have been performed based on the nonrelativistic density functional theory. On the relativistic side, many investigations have been done and significant progress has been made based on the covariant density functional theory [12,28–35].

The covariant density functional theory (CDFT) has been proved to be a powerful theory in nuclear physics by its successful description of many nuclear phenomena [1,30,36–42]. As a microscopic and covariant theory, the CDFT has attracted a lot of attention in recent years for many attractive advantages, such as the automatic inclusion of nucleonic spin degree of freedom, explaining naturally the pseudospin symmetry in the nucleon spectrum [43–48] and the spin symmetry in antinucleon spectrum [48–50], and the natural inclusion of nuclear magnetism [51], which plays an important role in nuclear magnetic moments [52–56] and nuclear rotations [30,57–67].

Based on the CDFT, assuming the spherical symmetry and taking into account both bound states and continuum via the Bogoliubov transformation in a microscopic and self-consistent way, the relativistic continuum Hartree-Bogoliubov (RCHB) theory was developed in Refs. [68,69] with the relativistic Hartree-Bogoliubov equations solved in the coordinate space. With the pairing correlation and the coupling to the continuum considered, the RCHB theory has achieved great success in reproducing and interpreting the halo in ^{11}Li [68], predicting the giant halo phenomena [70–72], reproducing the interaction cross section and charge-changing cross sections in sodium isotopes [73] and other light exotic nuclei [74], interpreting the pseudospin symmetry in exotic nuclei [44,45], and making predictions of new magic numbers in superheavy nuclei [75] and neutron halos in hypernuclei [76]. Recently, based on the RCHB theory with point-coupling density functional PC-PK1 [77], the first nuclear mass table including continuum effects was constructed and the continuum effects on the limits of the nuclear landscape were studied [12]. It was demonstrated that the continuum effects are crucial for drip-line locations and there are totally 9035 nuclei with $8 \leqslant Z \leqslant 120$ predicted to be bound, which remarkably extends the existing nuclear landscape. The RCHB mass table has

been applied to investigate α-decay energies [78] and proton radioactivity [79].

Except for doubly-magic nuclei, most nuclei in the nuclear chart deviate from spherical shape. Solving the deformed relativistic Hartree-Bogoliubov equations in the coordinate space is extremely difficult if not impossible [80]. To provide a proper description of deformed exotic nuclei, the deformed relativistic Hartree-Bogoliubov theory in continuum (DRHBc) based on the meson-exchange density functional was developed in Refs. [81,82], with the deformed relativistic Hartree-Bogoliubov equations solved in a Dirac Woods-Saxon basis [83]. Inheriting the advantages of RCHB theory and including the deformation degree of freedom, the DRHBc theory was applied to study magnesium isotopes, and an interesting shape decoupling between the core and the halo was predicted in ^{44}Mg and ^{42}Mg [81,82]. The DRHBc theory has been extended to a version with density-dependent meson-nucleon couplings [84] and to incorporate the blocking effect [85]. The success of DRHBc theory has been demonstrated in resolving the puzzles concerning the radius and configuration of valence neutrons in ^{22}C [86] and studying particles in the classically forbidden regions for magnesium isotopes [87].

The deformation plays an important role in the description of nuclear masses and affects the location of the neutron drip line [12]. It is therefore necessary to construct an upgraded mass table including simultaneously the deformation and continuum effects using the DRHBc theory.

It is quite challenging to include both the deformation and continuum effects in coordinate space. In the DRHBc theory, the coupled relativistic Hartree-Bogoliubov equations are solved by expansion on a spherical Dirac Woods-Saxon basis [83], with the Woods-Saxon parameters taken from Ref. [88]. It is numerically much more complicated than the RCHB theory. So far, the DRHBc theory has been applied to light nuclei only [81,82,84–87]. In order to provide a unified

description for all nuclei in the nuclear chart with the DRHBc theory, the difficulties include justifying a unified numerical setting, locating the ground-state deformation, and blocking the correct orbit(s) for odd-A and odd-odd nuclei. Blocking the correct orbit for an odd-A nucleus means that calculation should be performed by blocking several orbits near the Fermi level of its neighboring even-even nucleus independently and the one with the lowest energy should be identified [12,85,89]. The blocking procedure for an odd-odd nucleus is similar to that for the odd-A nuclei, but requires blocking both the proton and neutron levels at the same time. Last but not the least, so far the DRHBc theory is based on the meson-exchange density functionals. It is necessary to develop the DRHBc theory with point-coupling density functionals to adopt the successful PC-PK1.

In this work, the DRHBc theory based on the point-coupling density functionals is developed and its application for even-even nuclei is discussed in detail. The formalism is presented in Sec. II. Numerical checks are performed from light nuclei to heavy nuclei, and the details to construct a DRHBc mass table for even-even nuclei are suggested in Sec. III. As examples, the DRHBc calculated results for neodymium isotopes are compared with the RCHB mass table [12] and the available data [15,90,91] in Sec. IV. A summary is given in Sec. V.

II. THEORETICAL FRAMEWORK

The DRHBc theory based on the meson-exchange density functionals has been developed [81] and the details can be found in Ref. [82]. In this paper the DRHBc theory with point-coupling density functionals is developed and its formalism is presented in the following in brief.

The point-coupling density functional starts from the following Lagrangian density [1]:

$$
\begin{aligned}
\mathcal{L} = {}& \bar{\psi}(i\gamma_\mu \partial^\mu - M)\psi - \frac{1}{2}\alpha_S(\bar{\psi}\psi)(\bar{\psi}\psi) - \frac{1}{2}\alpha_V(\bar{\psi}\gamma_\mu\psi)(\bar{\psi}\gamma^\mu\psi) - \frac{1}{2}\alpha_{TV}(\bar{\psi}\vec{\tau}\gamma_\mu\psi)(\bar{\psi}\vec{\tau}\gamma^\mu\psi) \\
& - \frac{1}{2}\alpha_{TS}(\bar{\psi}\vec{\tau}\psi)(\bar{\psi}\vec{\tau}\psi) - \frac{1}{3}\beta_S(\bar{\psi}\psi)^3 - \frac{1}{4}\gamma_S(\bar{\psi}\psi)^4 - \frac{1}{4}\gamma_V[(\bar{\psi}\gamma_\mu\psi)(\bar{\psi}\gamma^\mu\psi)]^2 \\
& - \frac{1}{2}\delta_S\partial_\nu(\bar{\psi}\psi)\partial^\nu(\bar{\psi}\psi) - \frac{1}{2}\delta_V\partial_\nu(\bar{\psi}\gamma_\mu\psi)\partial^\nu(\bar{\psi}\gamma^\mu\psi) - \frac{1}{2}\delta_{TV}\partial_\nu(\bar{\psi}\vec{\tau}\gamma_\mu\psi)\partial^\nu(\bar{\psi}\vec{\tau}\gamma^\mu\psi) \\
& - \frac{1}{2}\delta_{TS}\partial_\nu(\bar{\psi}\vec{\tau}\psi)\partial^\nu(\bar{\psi}\vec{\tau}\psi) - \frac{1}{4}F^{\mu\nu}F_{\mu\nu} - e\bar{\psi}\gamma^\mu\frac{1-\tau_3}{2}A_\mu\psi,
\end{aligned}
\tag{1}
$$

where M is the nucleon mass, e is the charge unit, and A_μ and $F_{\mu\nu}$ are the four-vector potential and field strength tensor of the electromagnetic field, respectively. Here α_S, α_V, α_{TS}, and α_{TV} represent the coupling constants for four-fermion terms, β_S, γ_S, and γ_V are those for the higher-order terms which are responsible for the medium effects, and δ_S, δ_V, δ_{TS}, and δ_{TV} refer to those for the gradient terms, which are included to simulate the finite-range effects. The subscripts S, V, and T stand for scalar, vector, and isovector, respectively. The isovector-scalar channel including the terms α_{TS} and

δ_{TS} in Eq. (1) is neglected since including the isovector-scalar interaction does not improve the description of nuclear ground-state properties [92].

From the Lagrangian density of Eq. (1), the energy density functional for the nuclear system can be constructed under the mean-field and no-sea approximations. By minimizing the energy density functional with respect to the densities, one obtains the Dirac equation for nucleons within the relativistic mean-field framework [1]. The pairing correlation is crucial in the description of open-shell nuclei. The conventional BCS

theory used extensively in describing the pairing correlation turns out to be an insufficient approach for exotic nuclei [93]. The relativistic Hartree-Bogoliubov (RHB) theory can provide a unified and self-consistent treatment of both the mean field and the pairing correlation [69,94–96], and can describe the exotic nuclei properly in the coordinate space [69] or a Dirac Woods-Saxon basis [81].

The RHB equation reads

$$\begin{pmatrix} \hat{h}_D - \lambda_\tau & \hat{\Delta} \\ -\hat{\Delta}^* & -\hat{h}_D^* + \lambda_\tau \end{pmatrix} \begin{pmatrix} U_k \\ V_k \end{pmatrix} = E_k \begin{pmatrix} U_k \\ V_k \end{pmatrix}, \quad (2)$$

where $\hat{h}_D$ is the Dirac Hamiltonian, $\hat{\Delta}$ is the pairing field, λ_τ is the Fermi energy for neutron or proton ($\tau = n, p$), E_k is the quasiparticle energy, and U_k and V_k are the quasiparticle wave functions.

The Dirac Hamiltonian in the coordinate space is

$$h_D(\mathbf{r}) = \boldsymbol{\alpha} \cdot \mathbf{p} + V(\mathbf{r}) + \beta[M + S(\mathbf{r})], \quad (3)$$

with the scalar and vector potentials

$$S(\mathbf{r}) = \alpha_S \rho_S + \beta_S \rho_S^2 + \gamma_S \rho_S^3 + \delta_S \Delta \rho_S, \quad (4)$$

$$V(\mathbf{r}) = \alpha_V \rho_V + \gamma_V \rho_V^3 + \delta_V \Delta \rho_V + eA^0 + \alpha_{TV} \tau_3 \rho_3 \\ + \delta_{TV} \tau_3 \Delta \rho_3, \quad (5)$$

constructed by various densities:

$$\rho_S(\mathbf{r}) = \sum_{k>0} V_k^\dagger(\mathbf{r}) \gamma_0 V_k(\mathbf{r}),$$

$$\rho_V(\mathbf{r}) = \sum_{k>0} V_k^\dagger(\mathbf{r}) V_k(\mathbf{r}), \quad (6)$$

$$\rho_3(\mathbf{r}) = \sum_{k>0} V_k^\dagger(\mathbf{r}) \tau_3 V_k(\mathbf{r}).$$

According to the no-sea approximation, the summations in the above equations are performed over the quasiparticle states with positive energies in the Fermi sea.

The pairing potential is

$$\Delta(\mathbf{r}_1 s_1 p_1, \mathbf{r}_2 s_2 p_2) = \sum_{s_1' p_1'}^{s_2' p_2'} V^{pp}(\mathbf{r}_1, \mathbf{r}_2; s_1 p_1, s_2 p_2, s_1' p_1', s_2' p_2') \\ \times \kappa(\mathbf{r}_1 s_1' p_1', \mathbf{r}_2 s_2' p_2'), \quad (7)$$

where s represents the spin degree of freedom, p represents the upper or lower component of the Dirac spinors, $\kappa(\mathbf{r}_1 s_1' p_1', \mathbf{r}_2 s_2' p_2')$ is the pairing tensor [89], and V^{pp} is the pairing interaction in the particle-particle channel. Here a density-dependent zero-range pairing force is adopted,

$$V^{pp}(\mathbf{r}_1, \mathbf{r}_2) = V_0 \frac{1}{2}(1 - P^\sigma)\delta(\mathbf{r}_1 - \mathbf{r}_2)\left(1 - \frac{\rho(\mathbf{r}_1)}{\rho_{\text{sat}}}\right), \quad (8)$$

with V_0 the pairing strength, ρ_{sat} the saturation density of nuclear matter, and $\frac{1}{2}(1 - P^\sigma)$ the projector for the spin $S = 0$ component in the pairing channel. Details of the calculations of the pairing tensor and pairing potential can be found in Ref. [82].

For axially deformed nuclei, the potentials in Eqs. (4) and (5) together with densities in Eq. (6) are expanded in terms

of the Legendre polynomials [97]

$$f(\mathbf{r}) = \sum_\lambda f_\lambda(r) P_\lambda(\cos\theta), \quad \lambda = 0, 2, 4, \dots, \quad (9)$$

with

$$f_\lambda(r) = \frac{2\lambda + 1}{4\pi} \int d\Omega f(\mathbf{r}) P_\lambda(\Omega). \quad (10)$$

Because of the spatial reflection symmetry, λ is restricted to be even numbers.

For exotic nuclei with Fermi energy very close to the continuum threshold, the pairing interaction can scatter nucleons from bound states to the resonant states in the continuum. The density could become more diffuse due to this coupling to the continuum, and the position of the drip line might be influenced, which is the so-called continuum effect. In order to take into account the continuum effects, the deformed RHB equations are solved in a spherical Dirac Woods-Saxon basis, in which the radial wave functions have a proper asymptotic behavior for large r [83]. For techniques to treat strictly the boundary condition for the continuum, see Refs. [98–101].

The Dirac Woods-Saxon basis is obtained by solving a Dirac equation with spherical Woods-Saxon scalar and vector potentials [83,88]. The basis wave function reads

$$\varphi_{n\kappa m}(\mathbf{r}s) = \frac{1}{r} \begin{pmatrix} iG_{n\kappa}(r) Y_{jm}^l(\Omega s) \\ -F_{n\kappa}(r) Y_{jm}^{\tilde{l}}(\Omega s) \end{pmatrix}, \quad (11)$$

with $G_{n\kappa}(r)/r$ and $F_{n\kappa}(r)/r$ the radial wave functions for large and small components, and $Y_{jm}^{l(\tilde{l})}(\Omega s)$ the spin spherical harmonics, where n is the radial quantum number, $\kappa = (-1)^{j+l+1/2}(j + 1/2)$, and $\tilde{l} = l + (-1)^{j+l-1/2}$. For completeness of the basis, the solutions in the Dirac sea should also be included in the basis space [83].

With a set of complete Dirac Woods-Saxon bases, solving the RHB equation (2) is equivalent to the diagonalization of the RHB matrix. Symmetries can simplify the calculation considerably. For axially deformed nuclei with spatial reflection symmetry, the parity π and the projection of the angular momentum on the symmetry axis m are good quantum numbers. Therefore, the RHB matrix can be decomposed into different m^π blocks. Moreover, because of time-reversal symmetry, one only needs to diagonalize the RHB matrix in each positive-m block,

$$\begin{pmatrix} \mathcal{A} - \lambda_\tau & \mathcal{B} \\ \mathcal{B}^\dagger & -\mathcal{A}^* + \lambda_\tau \end{pmatrix} \begin{pmatrix} \mathcal{U}_k \\ \mathcal{V}_k \end{pmatrix} = E_k \begin{pmatrix} \mathcal{U}_k \\ \mathcal{V}_k \end{pmatrix}, \quad (12)$$

where the matrix elements are

$$\mathcal{A} = \left(h_{D(n\kappa)(n'\kappa')}^{(m)}\right) = (\langle n\kappa m|h_D|n'\kappa'm\rangle), \quad (13)$$

$$\mathcal{B} = \left(\Delta_{(n\kappa)(n'\kappa')}^{(m)}\right) = (\langle n\kappa m|\Delta|\overline{n'\kappa'm}\rangle). \quad (14)$$

For odd systems, the equal filling approximation that conserves time-reversal symmetry is adopted [85]. The details of the calculation of RHB matrix elements can be found in Ref. [82]. The obtained eigenvectors correspond to the expansion coefficients of quasiparticle wave functions in the Dirac Woods-Saxon basis

$$\mathcal{U}_k = \left(u_{k,(n\kappa)}^{(m)}\right), \qquad \mathcal{V}_k = \left(v_{k,(n\kappa)}^{(m)}\right). \quad (15)$$

From these quasiparticle wave functions, new densities and potentials can be obtained, which are iterated in the RHB equations until convergence is achieved.

Finally, one can calculate the total energy of a nucleus by [1,69]

$$
\begin{aligned}
E_{\text{RHB}} = & \sum_{k>0}(\lambda_\tau - E_k)v_k^2 - E_{\text{pair}} \\
& - \int d^3\boldsymbol{r}\bigg(\frac{1}{2}\alpha_S\rho_S^2 + \frac{1}{2}\alpha_V\rho_V^2 + \frac{1}{2}\alpha_{TV}\rho_3^2 \\
& + \frac{2}{3}\beta_S\rho_S^3 + \frac{3}{4}\gamma_S\rho_S^4 + \frac{3}{4}\gamma_V\rho_V^4 + \frac{1}{2}\delta_S\rho_S\Delta\rho_S \\
& + \frac{1}{2}\delta_V\rho_V\Delta\rho_V + \frac{1}{2}\delta_{TV}\rho_3\Delta\rho_3 + \frac{1}{2}\rho_p eA^0\bigg) + E_{\text{c.m.}},
\end{aligned}
$$

where

$$
v_k^2 = \int d^3\boldsymbol{r}V_k^\dagger(\boldsymbol{r})V_k(\boldsymbol{r}). \tag{17}
$$

For the zero-range pairing force, the pairing field $\Delta(\boldsymbol{r})$ is local, and the pairing energy is calculated as

$$
E_{\text{pair}} = -\frac{1}{2}\int d^3\boldsymbol{r}\kappa(\boldsymbol{r})\Delta(\boldsymbol{r}). \tag{18}
$$

The center-of-mass (c.m.) correction energy is calculated microscopically,

$$
E_{\text{c.m.}} = -\frac{1}{2mA}\langle\hat{\boldsymbol{P}}^2\rangle, \tag{19}
$$

with A the mass number and $\hat{\boldsymbol{P}} = \sum_i^A \hat{\boldsymbol{p}}_i$ the total momentum in the c.m. frame. It has been shown that the microscopic c.m. correction provides more reasonable and reliable results than phenomenological ones [102–104].

For deformed nuclei, as the rotational symmetry is broken in the mean-field approximation, the rotational correction energy, i.e., the energy gained by the restoration of rotational symmetry, should also be included properly [77]. Here the rotational correction energy is obtained from the cranking approximation,

$$
E_{\text{rot}} = -\frac{1}{2\mathscr{I}}\langle\hat{\boldsymbol{J}}^2\rangle, \tag{20}
$$

where $\mathscr{I}$ is the moment of inertia calculated by the Inglis-Belyaev formula [89] and $\hat{\boldsymbol{J}} = \sum_i^A \hat{\boldsymbol{j}}_i$ is the total angular momentum.

The root-mean-square (rms) radius is calculated as

$$
R_{\tau,\text{rms}} = \langle r^2\rangle^{1/2} = \sqrt{\frac{\int d^3\boldsymbol{r}[r^2\rho_\tau(\boldsymbol{r})]}{N_\tau}}, \tag{21}
$$

where τ represents the proton, the neutron, or the nucleon, and ρ_τ is the corresponding vector density, and N_τ refers to the corresponding particle's number. The rms charge radius is simply calculated as

$$
R_c = \sqrt{R_{p,\text{rms}}^2 + 0.64 \text{ fm}^2}. \tag{22}
$$

The intrinsic quadrupole moment is calculated by

$$
Q_{\tau,2} = \sqrt{\frac{16\pi}{5}}\langle r^2 Y_{20}(\theta,\varphi)\rangle. \tag{23}
$$

The quadrupole deformation parameter is obtained from the quadrupole moment by

$$
\beta_{\tau,2} = \frac{\sqrt{5\pi}Q_{\tau,2}}{3N_\tau\langle r_\tau^2\rangle}. \tag{24}
$$

The canonical basis $|\psi_i\rangle$ can be obtained by diagonalizing the density matrix $\hat{\rho}$ [89],

$$
\hat{\rho}|\psi_i\rangle = v_i^2|\psi_i\rangle, \tag{25}
$$

where the eigenvalue v_i^2 is the corresponding occupation probability of $|\psi_i\rangle$. It has to be emphasized that, in a diagonalization problem, the degeneration of eigenvalues will lead to an arbitrary mixture of the eigenvectors that satisfies the unitary transformation in the corresponding subspace. As a consequence, the canonical states are not uniquely defined when their occupation probabilities are degenerate. The problem can be solved by diagonalizing $\hat{h}_D$ in the subspace with degenerate occupation probabilities to determine the canonical single-particle states uniquely [1].

III. NUMERICAL DETAILS

Here we concentrate on the numerical details in the systematic calculations for even-even nuclei from the proton drip lines to the neutron drip lines in the nuclear chart with the DRHBc theory. For the particle-hole channel, the relativistic density functional PC-PK1 [77], which has turned out to be very successful in providing good descriptions of the isospin dependence of the binding energy along both the isotopic and the isotonic chains [31,34,105], is adopted. For the particle-particle channel, the density-dependent zero-range pairing force in Eq. (8) is used.

In the DRHBc theory, the relativistic Hartree-Bogoliubov equations are solved by expansion on a spherical Dirac Woods-Saxon basis [83], with the Woods-Saxon parameters taken from Ref. [88]. Therefore, the box size R_{box} and the mesh size Δr for the Dirac Woods-Saxon basis should be determined. Second, for completeness of the basis space, an angular momentum cutoff J_{max}, an energy cutoff E_{cut}^+ for the Woods-Saxon basis in the Fermi sea, and the number of states in the Dirac sea should be chosen properly. Third, the convergence of Legendre expansion in Eq. (9) for the deformed densities and potentials should be guaranteed. Finally, the pairing strength in Eq. (8) should be justified properly.

In Ref. [83], the solutions of Dirac equations in the Dirac Woods-Saxon basis with $R_{\text{box}} = 20$ fm and $\Delta r = 0.1$ fm reproduce accurately the results obtained by the shooting method. In the RCHB mass table [12], $R_{\text{box}} = 20$ fm and $\Delta r = 0.1$ fm have been chosen. Here we have further checked the convergence of DRHBc solutions with respect to R_{box} and Δr for deformed nuclei ^{20}Ne, ^{112}Mo, and ^{300}Th, and found that $R_{\text{box}} = 20$ fm and $\Delta r = 0.1$ fm lead to a satisfactory accuracy of less than 0.01% of the binding energies. Therefore,
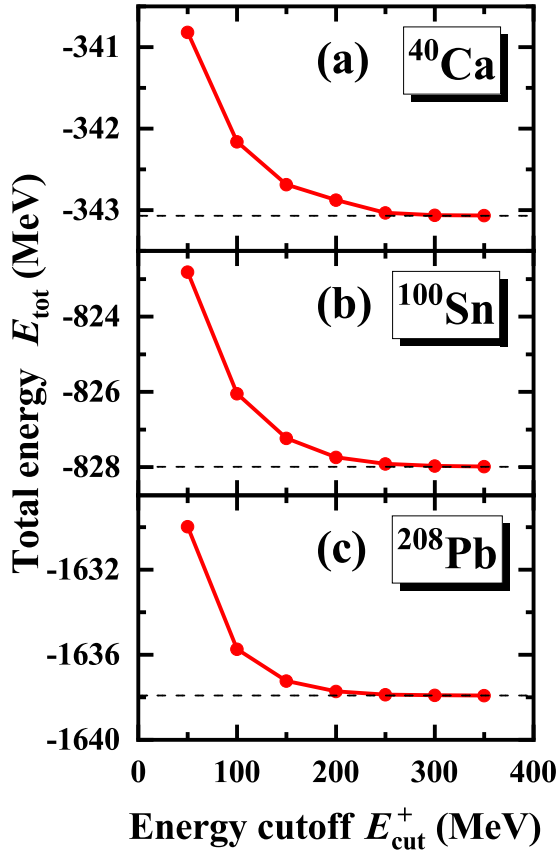
FIG. 1. Total energy as a function of the energy cutoff E_{cut}^+ for doubly-magic nuclei ^{40}Ca (a), ^{100}Sn (b), and ^{208}Pb (c) calculated by the DRHBc theory. Dashed lines show total energies of these three nuclei in the RCHB mass table [12]. As in the RCHB calculations [12], the angular momentum cutoff $J_{max} = 19/2\hbar$ is used here.

the box size $R_{box} = 20$ fm and the mesh size $\Delta r = 0.1$ fm are used in the present DRHBc calculations.

In the following, numerical checks for the energy cutoff E_{cut}^+ and the angular momentum cutoff J_{max} will be performed. The number of states in the Dirac sea is taken to be the same as that in the Fermi sea [81–83]. A convergence check for the Legendre expansion will also be performed. In addition, the pairing strength will be determined by reproducing experimental odd-even mass differences, and the strategy to determine ground states in the DRHBc calculations will be suggested according to the self-consistency between unconstrained and constrained calculations.

A. Energy cutoff for Woods-Saxon basis

In Ref. [83], it is found that the results of calculations with the Dirac Woods-Saxon basis converge to the exact ones with the energy cutoff $E_{cut}^+ \approx 300$ MeV. Here we perform fully self-consistent calculations to examine the convergence of total energy with the energy cutoff E_{cut}^+, as seen in Fig. 1, for doubly-magic nuclei ^{40}Ca, ^{100}Sn, and ^{208}Pb. The results from the RCHB mass table [12] are also shown for comparison. The total energy of each nucleus converges gradually to the corresponding RCHB result with increasing E_{cut}^+. When $E_{cut}^+ =$
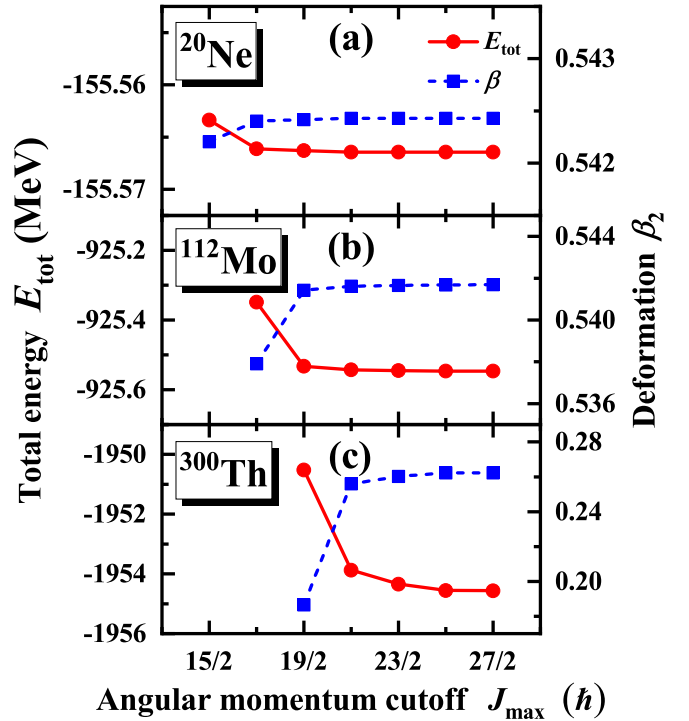

FIG. 2. Total energy and deformation versus the angular momentum cutoff J_{max} for deformed nuclei ^{20}Ne (a), ^{112}Mo (b), and ^{300}Th (c), with the energy cutoff $E_{cut}^+ = 300$ MeV. Here the pairing correlation is neglected.

300 MeV, the total energy differences between the DRHBc and RCHB calculations for ^{40}Ca, ^{100}Sn, and ^{208}Pb are 0.0097, 0.0193, and 0.0179 MeV, respectively. Changing E_{cut}^+ from 300 to 350 MeV, the total energy varies by 0.0037, 0.0090, and 0.0093 MeV for ^{40}Ca, ^{100}Sn, and ^{208}Pb, respectively. Therefore, consistent with the conclusion in Ref. [83] and the RCHB mass table [12], $E_{cut}^+ = 300$ MeV is a reasonable choice for the DRHBc mass table calculations.

B. Angular momentum cutoff

In the RCHB mass table calculations, the convergence has been confirmed for the angular momentum cutoff $J_{max} = 19/2\hbar$ [12]. With deformation effects included in DRHBc calculations, further numerical checks for J_{max} are necessary.

Figure 2 shows the total energy and deformation versus the angular momentum cutoff J_{max} for deformed nuclei ^{20}Ne, ^{112}Mo, and ^{300}Th, where $E_{cut}^+ = 300$ MeV and the pairing is neglected. The stable light nucleus ^{20}Ne, short-lived medium-heavy nucleus ^{112}Mo, and neutron-rich heavy nucleus ^{300}Th are chosen in order to determine a universal angular momentum cutoff. It is found that $J_{max} = 19/2\hbar$ is enough for light nuclei like ^{20}Ne and medium-heavy nuclei like ^{112}Mo. For heavy nucleus ^{300}Th, changing J_{max} from $19/2\hbar$ to $27/2\hbar$, the deformation varies by about 0.08 and the total energy varies by 4.0406 MeV. Changing J_{max} from $23/2\hbar$ to $27/2\hbar$, the deformation varies by about 0.002 and the total energy varies by 0.2180 MeV, which is about 0.01% of its total energy. Therefore, a unified angular momentum cutoff $J_{max} = 23/2\hbar$
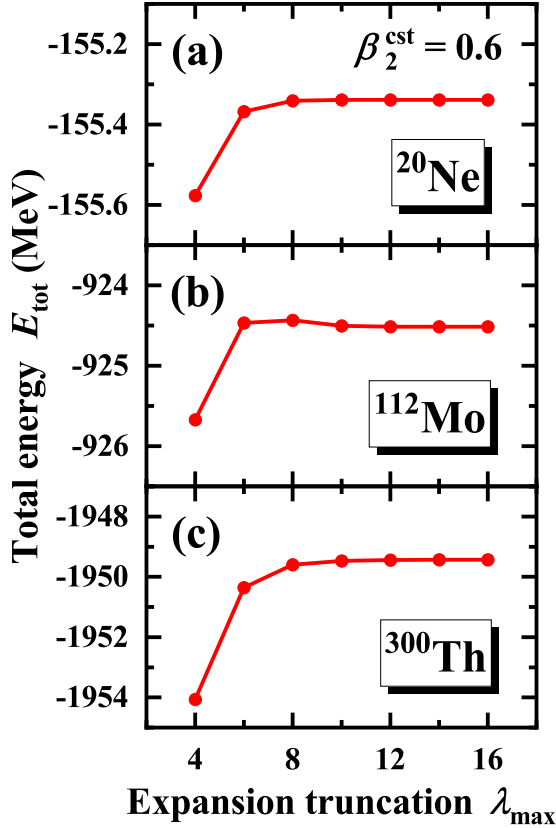
FIG. 3. Total energy as a function of the Legendre expansion truncation λ_{max} for nuclei ^{20}Ne (a), ^{112}Mo (b), and ^{300}Th (c) from constrained DRHBc calculations at the quadrupole deformation $\beta_2 = 0.6$, with the energy cutoff $E_{cut}^+ = 300$ MeV and the angular momentum cutoff $J_{max} = 23/2\hbar$. Here the pairing correlation is neglected.

is suggested in the DRHBc calculations in order to achieve a satisfactory accuracy for the entire nuclear landscape.

C. Legendre expansion

In the DRHBc theory, the deformed densities and potentials are expanded in terms of the Legendre polynomials as in Eq. (9) [81]. Since a nucleus with a large deformation may need higher orders in the Legendre expansion, the convergence of the expansion truncation λ_{max} is checked for nuclei ^{20}Ne, ^{112}Mo, and ^{300}Th at the constrained deformation $\beta_2 = 0.6$. Figure 3 shows the total energies as a function of the Legendre expansion truncation λ_{max} for ^{20}Ne, ^{112}Mo, and ^{300}Th. Changing λ_{max} from 6 to 16, the total energy varies by 0.03 MeV for ^{20}Ne and 0.05 MeV for ^{112}Mo, i.e., less than 0.03% of their total energies. Changing λ_{max} from 8 to 16, the total energy of ^{300}Th varies by 0.16 MeV, i.e., less than 0.01% of its total energy. Therefore, in the mass table calculations, for light nuclei like ^{20}Ne and medium-heavy nuclei like ^{112}Mo, $\lambda_{max} = 6$ can provide converged results. For heavy nuclei like ^{300}Th, $\lambda_{max} = 8$ is necessary in order to achieve convergence. Although the pairing correlation is neglected, the conclusion is also valid after the inclusion of the pairing correlation [106].
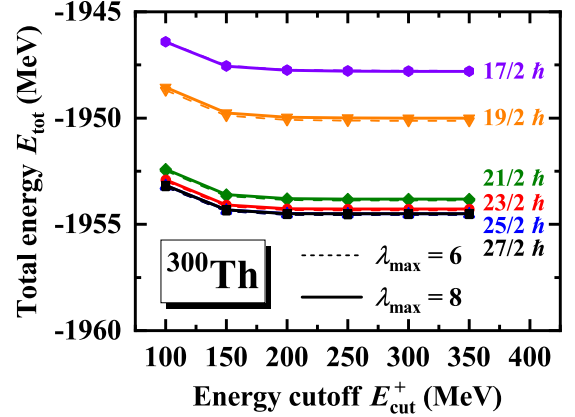

FIG. 4. The convergence of the total energy in ^{300}Th with the energy cutoff, for angular momentum cutoff from $17/2\hbar$ to $27/2\hbar$, in which the Legendre expansion truncation $\lambda_{max} = 6$ and 8, labeled by dashed and solid lines, respectively. Here the pairing correlation is neglected.

In order to confirm the above-obtained numerical settings, Fig. 4 shows the convergence of the total energy in ^{300}Th with respect to the energy cutoff, the angular momentum cutoff, and the Legendre expansion truncation simultaneously. For given angular momentum cutoff and Legendre expansion truncation, the energy difference is less than 0.01 MeV between $E_{cut}^+ = 300$ and 350 MeV. For given energy cutoff and Legendre expansion truncation, the energy difference is less than 0.27 MeV between $J_{max} = 23/2\hbar$ and $27/2\hbar$. For given energy cutoff and angular momentum cutoff, the energy difference is less than 0.13 MeV between $\lambda_{max} = 6$ and 8. Therefore, the suggested numerical settings obtained by the independent convergence check of each parameter are confirmed by varying all three parameters at the same time.

D. Pairing strength

In the present DRHBc calculations, the saturation density $\rho_{sat} = 0.152$ fm^{-3} in Eq. (8) is used. As in the calculations for the RCHB mass table [12], a cutoff energy 100 MeV in the quasiparticle space is used for the pairing window. With the angular momentum cutoff $J_{max} = 23/2\hbar$, the pairing strength is chosen to reproduce the experimental odd-even mass differences,

$$\Delta_n^{(3)} = \frac{(-1)^N}{2}[E_b(Z, N+1) - 2E_b(Z, N) + E_b(Z, N-1)]. \tag{26}$$

The odd-even mass differences in Ca and Pb isotopic chains are used to fix the pairing strength. As Ca and Pb isotopes are proton magic nuclei, spherical symmetry is assumed in the calculation, i.e., the Legendre expansion truncation is taken as $\lambda_{max} = 0$. We realize that some odd-mass isotopes [107–109] and some mid-shell neutron-deficient Pb isotopes [32] might not be spherical. As shown in Fig. 5, the experimental odd-even mass differences can be nicely reproduced. The pairing strength thus obtained will be used to construct the mass table.

Figure 5 shows the DRHBc calculated odd-even mass differences for Ca isotopes and Pb isotopes, the corresponding
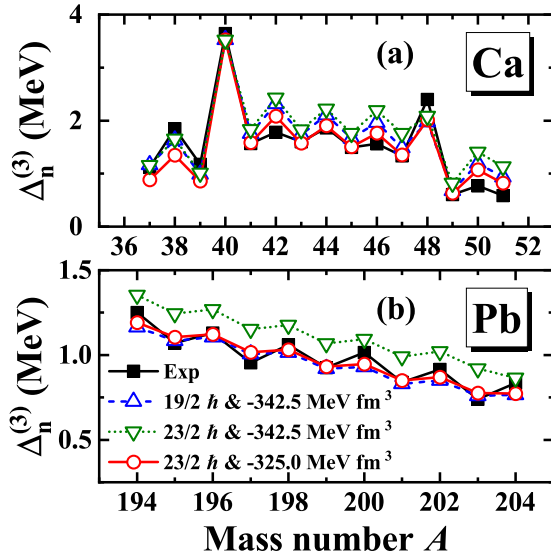
FIG. 5. Odd-even mass differences of Ca (a) and Pb (b) isotopic chains in the DRHBc calculations versus the mass number, for $V_0 = -342.5$ MeV fm^3 with $J_{max} = 23/2\hbar$ (inverted triangle) and for $V_0 = -325.0$ MeV fm^3 with $J_{max} = 23/2\hbar$ (circle). The corresponding experimental data [15] (square) and the results in the RCHB mass table [12] (triangle) are shown for comparison.

FIG. 6. Potential energy curve (PEC) of ^{130}Nd in constrained DRHBc calculations. The unconstrained results are also shown. Here the energy cutoff $E_{cut}^+ = 300$ MeV, the angular momentum cutoff $J_{max} = 23/2\hbar$, the Legendre expansion truncation $\lambda_{max} = 6$, and the pairing strength $V_0 = -325.0$ MeV fm^3 are used.

experimental data [15], as well as the results in the RCHB mass table [12]. For $J_{max} = 23/2\hbar$, if the pairing strength $V_0 = -342.5$ MeV fm^3 in Ref. [12] is adopted, the odd-even mass differences will be overestimated for most Ca and Pb isotopes. In order to reproduce the experimental values, $V_0 = -325.0$ MeV fm^3 should be adopted. Therefore, the pairing strength $V_0 = -325.0$ MeV fm^3 will be used in the DRHBc mass table calculations.

E. Constrained calculations

In order to describe the shape of the atomic nucleus and understand the shape coexistence, it is crucial to obtain the potential energy surface (PES) of the nucleus as a function of the deformation [41]. In microscopic models, there are two different ways to obtain the PES, i.e., the adiabatic and configuration-fixed (diabatic) approaches [110–114]. In the present DRHBc calculations, the adiabatic constrained calculation is adopted to obtain the potential energy curve (PEC) of the nucleus as a function of the quadrupole deformation, and the augmented Lagrangian method [115] is used.

For each nucleus, in order to find the ground state, the DRHBc calculations are performed with initial deformations $\beta_2 = -0.4, -0.2, 0.0, 0.2, 0.4$, and 0.6. The solution with the lowest total energy corresponds to the ground state. Sometimes the constrained calculation is also necessary if the PEC is very soft, or several local minima are close to each other. In present calculations, the rotational correction is added to the mean-field minimum instead of the PEC. In general, adding the rotational correction to the PEC will lead to different ground states, in particular for a nucleus with a soft PEC or shape coexistence, which requires beyond-mean-field investigation and is out of the scope of the present study.
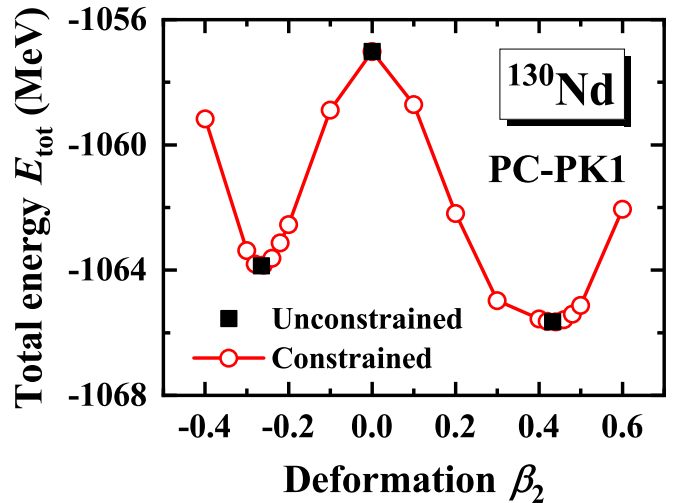
Taking ^{130}Nd as an example, the unconstrained calculations with different initial deformations respectively converge to $\beta_2 = -0.27$, 0.00, and 0.43, as shown in Fig. 6. The prolate solution has the lowest total energy and thus is considered to be the ground state. The constrained calculations are further performed for ^{130}Nd and shown in Fig. 6. Both the unconstrained prolate and oblate solutions correspond to the local minima in the PEC. Although the solution at $\beta_2 = 0.00$ is not a local minimum, the calculated total energy agrees with the constrained one. The self-consistency is therefore guaranteed and the strategy to find the ground state from unconstrained calculations is reasonable and practicable. Of course, whenever necessary, constrained calculations can be performed to build the PEC and confirm the ground state.

Summarizing the above discussions, the numerical details for the DRHBc mass table calculations including the box size $R_{box} = 20$ fm, the mesh size $\Delta r = 0.1$ fm, the energy cutoff $E_{cut}^+ = 300$ MeV, the angular momentum cutoff $J_{max} = 23/2\hbar$, the pairing strength $V_0 = -325.0$ MeV fm^3, and the sharp pairing window of 100 MeV are suggested. For Legendre expansion, the expansion truncation $\lambda_{max} = 6$ is suggested for $Z \leqslant 80$, and $\lambda_{max} = 8$ is suggested for $Z > 80$.

With the present numerical settings, a level of convergence up to 0.03% for the total energy can be expected for all nuclei at ground state with deformation in the region $-0.4 \leqslant \beta_2 \leqslant 0.6$. Taking the possible heaviest nucleus ^{400}120 as an example, the predicted ground-state binding energy at deformation $\beta_2 = 0.35$ is 2345.94 MeV, with an accuracy of 550 keV that is less than 0.03% of its binding energy. For ^{230}Hg, the predicted ground-state binding energy at deformation $\beta_2 = 0.30$ is 1707.18 MeV, with an accuracy of 50 keV that is less than 0.003% of its binding energy.
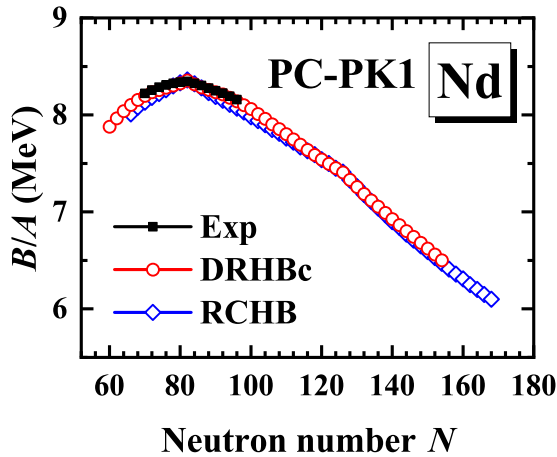
FIG. 7. Binding energy per nucleon of Nd isotopes from the DRHBc calculations as a function of the neutron number. The results in the RCHB mass table [12] and the experimental data from Ref. [15] are shown for comparison.

IV. RESULTS AND DISCUSSION

Taking even-even Nd isotopes as examples, the DRHBc calculations with the suggested numerical details in Sec. III are performed and the ground-state properties, such as binding energy, two-neutron separation energy, Fermi energy, quadrupole deformation, rms radius, density distribution, as well as the single-particle levels are obtained. In this section, ground-state properties of Nd isotopes will be discussed and compared with those predicted by the RCHB theory [12] and with available data [15,90,91]. The ground-state properties of even-even Nd isotopes are also tabulated in the Appendix.

A. Binding energy

In Fig. 7, the binding energies per nucleon for neodymium isotopes from the DRHBc calculations are shown versus the neutron number together with the RCHB results [12] and available data [15]. The most stable nucleus ^{142}Nd in neodymium isotopes with the magic number $N = 82$ is well reproduced by the DRHBc theory. Distinguishable differences between the DRHBc and the RCHB calculations can be seen. Away from the neutron shell closures 82 and 126, the deformation effects in the DRHBc calculations improve the RCHB results and reproduce better the data.

Figure 8 shows the differences between calculated binding energies and the available data [15]. The deformation effects in the DRHBc calculations dramatically reduce the deviation between the RCHB calculations and the data from up to 13.8 to less than 3.8 MeV. The rms deviation for the binding energy is reduced from 8.301 MeV in the RCHB calculations to 2.668 MeV in the DRHBc ones.

Following Ref. [77], the differences after including rotational correction energies in Eq. (20) in the DRHBc theory are also shown in Fig. 8. The largest deviation becomes less than 1.7 MeV and the rms deviation is reduced to 0.958 MeV. It should be noted that one can use the Thouless-Valatin formula to better estimate the moment of inertia in the calculation of rotation correction energy [27,116] and to examine if
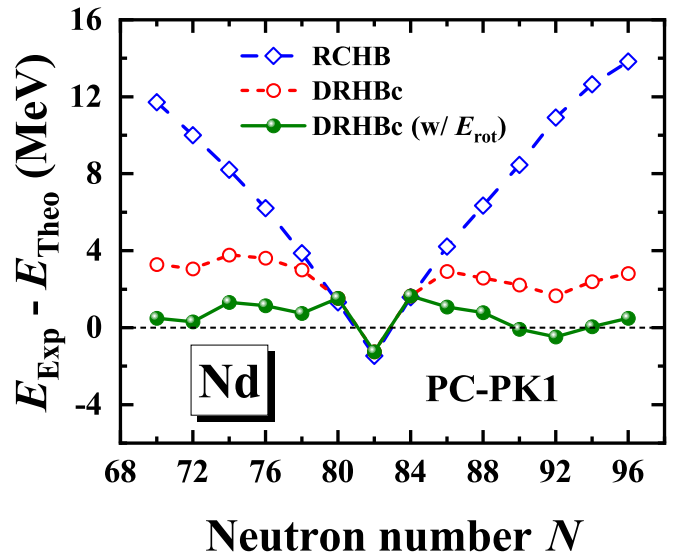

FIG. 8. The difference between the experimental binding energy [15] and the DRHBc calculations for Nd isotopes versus the neutron number. The results of the DRHBc calculations including rotational correction and the RCHB mass table [12] are also shown for comparison.

the rms deviation can be further reduced. Furthermore, the collective Hamiltonian method provides another method to better estimate the beyond-mean-field correlation energies as shown in Refs. [27,34,117].

The improved agreements between the calculated binding energies and the data by the deformation and beyond-mean-field correlation have been demonstrated by other density functional calculations as well. In Refs. [118,119], based on the Hartree-Fock plus BCS theory using the Skyrme SLy4 interaction and a density-dependent zero-range pairing force together with the generator coordinate method, total energies obtained from spherical, deformed, and beyond-mean-field calculations have been compared for 605 even-even nuclei. The rms deviations from the experimental data are respectively 11.7, 5.3, and 4.4 MeV for spherical, deformed, and beyond-mean-field calculations. In Ref. [27], based on the constrained-Hartree-Fock-Bogoliubov theory using the Gogny D1S interaction together with a five-dimensional collective Hamiltonian, total energies obtained from spherical, deformed, and beyond-mean-field calculations were compared for even-even nuclei with $10 \leqslant Z \leqslant 110$ and $N \leqslant 200$.

B. Two-neutron separation energy

From binding energies, the two-neutron separation energy can be calculated and the neutron drip line can be determined. Figure 9 shows the DRHBc and RCHB calculated two-neutron separation energies of neodymium isotopes, in comparison with the existing experimental data [15]. The DRHBc results are consistent with the RCHB ones for spherical nuclei near the neutron magic numbers $N = 82$ and $N = 126$. From ^{132}Nd to ^{140}Nd and ^{146}Nd to ^{156}Nd, the DRHBc calculations including deformation effects reproduce better the experimental values. From the DRHBc calculated
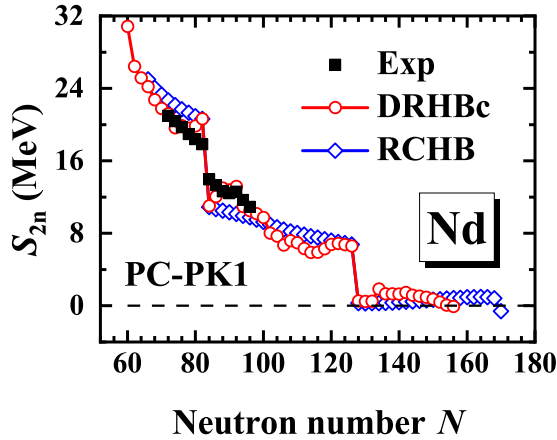
FIG. 9. Two-neutron separation energy as a function of the neutron number for Nd isotopes in the DRHBc calculations. The RCHB results [12] and the available data [15] are also shown for comparison.

two-neutron separation energies, the neutron drip-line (last bound) nucleus is predicted to be ^{214}Nd, while it is ^{228}Nd in the RCHB theory [12]. Including the deformation degrees of freedom, the predicted neutron drip-line location varies by 14 neutrons. It is of interest to investigate the deformation effects on drip-line locations over the whole nuclear landscape.

C. Fermi energy

The Fermi energy represents the change of the total energy for a change in the particle number [89]. In addition to the two-neutron separation energy, the Fermi energy can also provide information about the nucleon drip line. Figure 10 shows the neutron and proton Fermi energies in the DRHBc
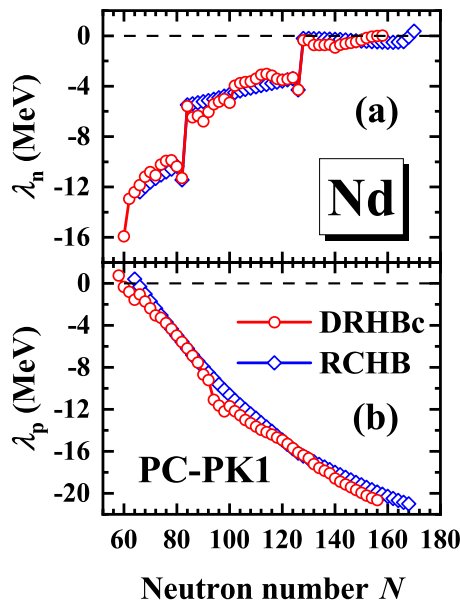

FIG. 10. Neutron (a) and proton (b) Fermi energies for Nd isotopes in the DRHBc calculations versus the neutron number. The results from the RCHB mass table [12] are shown for comparison.
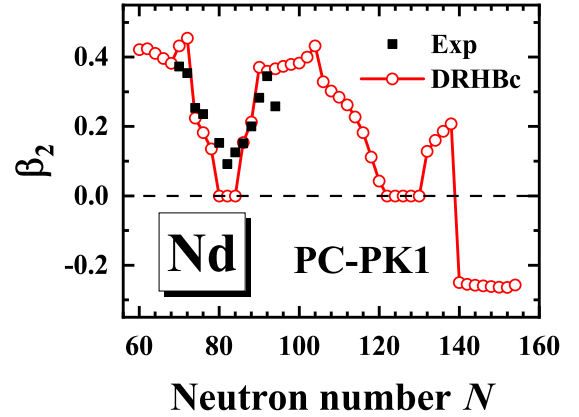

FIG. 11. Quadrupole deformation as a function of the neutron number in the DRHBc calculations for Nd isotopes. The available data [90] are shown for comparison.

calculations, in comparison with the RCHB results [12]. If the pairing energy vanishes, the Fermi energy is chosen to be the energy of the last occupied single-particle state. In Fig. 10(a), the neutron Fermi energy becomes positive at ^{218}Nd and ^{230}Nd in the RCHB ones. In the DRHBc calculations, although the neutron Fermi energy for ^{216}Nd is negative with $\lambda_n = -0.025$ MeV, it is unstable against neutron emission with $S_{2n} = -0.057$ MeV in Fig. 9. In the RCHB calculations, the neutron drip line from the Fermi energy is consistent with the two-neutron separation energies. The sudden increases in the neutron Fermi energy reflect the shell closures at $N = 82$ and $N = 126$. In Fig. 10(b), the proton Fermi energy becomes positive at ^{118}Nd in the DRHBc calculations and ^{124}Nd in the RCHB ones. Therefore, the deformation effects influence not only the neutron but also the proton drip line for neodymium isotopes. Near $N = 82$ and 126, the Fermi energies in the DRHBc calculations agree more or less with the RCHB ones. Moving away from the shell closures, the smooth evolution of Fermi energy does not exist in the DRHBc calculations due to deformation effects.

D. Quadrupole deformation

The ground-state quadrupole deformation parameters in Eq. (24) in the DRHBc calculations for neodymium isotopes are shown in Fig. 11 and compared with the available data [90]. Generally, the DRHBc calculated ground-state quadrupole deformations reproduce the data well. There exists some difference between the calculated deformation and the data, which might be explained by the fact that the data are not directly observed. The deformation data in Ref. [90] are extracted from the observed $B(E2, 0_1^+ \rightarrow 2_1^+)$ with the assumption of the nucleus as a rigid rotor, which might not be true for all nuclei. The nuclei near $N = 82$ and $N = 126$ exhibit spherical shape due to the shell effects. For these nuclei, the bulk properties in the DRHBc calculations discussed above are consistent with the RCHB ones. The shape evolution is the following: (a) from the proton drip line to $N = 80$, the shape changes from prolate to spherical; (b) from $N = 84$ to $N = 122$, the shape changes from spherical
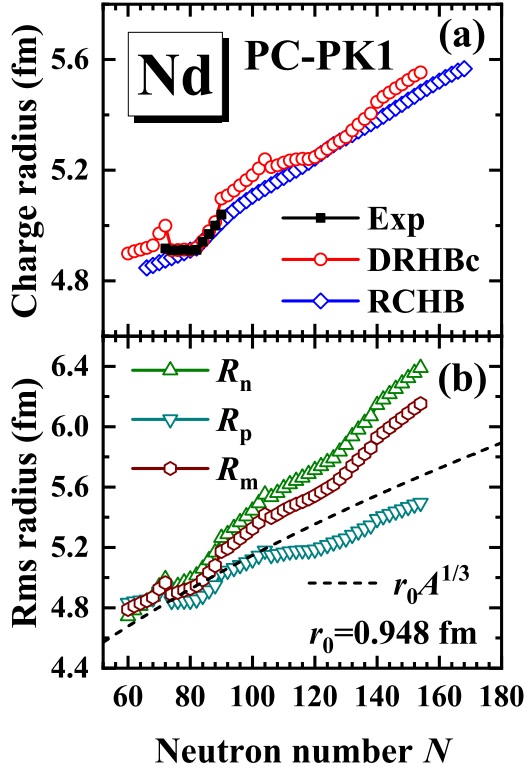
FIG. 12. (a) Charge radius as a function of the neutron number in the DRHBc calculations for Nd isotopes. The results in the RCHB mass table [12] and existing data from Ref. [91] are shown for comparison. (b) rms neutron radius, proton radius, and matter radius as functions of the neutron number in the DRHBc calculations for Nd isotopes. The empirical matter radii $r_0A^{1/3}$, in which $r_0 = 0.948$ fm determined by ^{142}Nd, are also shown to guide the eye.

to prolate and then back to spherical; (c) from $N = 130$ to $N = 138$, the shape changes from spherical to prolate; (d) from $N = 140$ to the neutron drip line, the shape changes to oblate.

E. rms radii

In Fig. 12(a), the charge radius as a function of the neutron number in the DRHBc calculations for neodymium isotopes are shown, together with the RCHB results [12] and the available data [91]. In general, the data are reproduced well by both the RCHB and DRHBc calculations. In particular, the DRHBc calculations reproduce well not only the data from ^{134}Nd to ^{148}Nd but also the kink at ^{142}Nd, in which the deformation plays a crucial role. For ^{132}Nd and ^{150}Nd, the charge radii are underestimated by the RCHB calculations due to the neglect of deformation, and are slightly overestimated by the DRHBc ones due to the overestimated deformation in Fig. 11. The overestimation of deformation for ^{132}Nd and ^{150}Nd might be due to their soft PESs, shown in Refs. [120,121].

In Fig. 12(b), the rms neutron radii R_n, proton radii R_p, and matter radii R_m in the DRHBc calculations for neodymium isotopes are shown. The empirical matter radii $r_0A^{1/3}$ with r_0 determined by the most stable neodymium isotope ^{142}Nd are shown to guide the eye. Starting from the proton drip line, R_n,

R_p, and R_m are close to each other and gradually increase with the neutron number. There is a sudden decrease from ^{132}Nd to ^{134}Nd because the quadrupole deformation parameter β_2 decreases from 0.46 to 0.23. Beyond ^{134}Nd, the proton radius increases gradually, the neutron radius increases more rapidly, and the matter radius is in between. By scaling the empirical matter radius $r_0A^{1/3}$ by the most stable nucleus ^{142}Nd, for the nuclei far away from the stability line, the calculated radii are systematically larger than the empirical ones. In particular, for nuclei with $N > 126$, the ever increasing deviation from the empirical value may indicate some underlying exotic structure.

F. Neutron density distribution

Figure 13 shows neutron density profiles of selected even-even neodymium isotopes $^{124,134,...,214}$Nd. In Fig. 13(a), $\rho_{n,0}$ represents the spherical component of the neutron density distribution [cf. Eq. (9)]. In Figs. 13(b) and 13(c), the total neutron density distributions along ($\theta = 0°$) and perpendicular ($\theta = 90°$) to the symmetry axis z are shown, respectively. In Fig. 13(a), for the spherical component, the neutron density distribution becomes more diffuse monotonically with the increasing mass number. In Figs. 13(b) and 13(c), the neutron density distributions manifest not only the diffuseness with the increasing neutron number but also the deformation effects. In Fig. 13(b), although ^{134}Nd has ten more neutrons than ^{124}Nd, its density along the symmetry axis is smaller than that of ^{124}Nd for $z \gtrsim 6$ fm. This can be understood from the deformation $\beta_2 = 0.41$ for ^{124}Nd and $\beta_2 = 0.23$ for ^{134}Nd. Due to their oblate deformation, the densities perpendicular to the symmetry axis for ^{204}Nd and ^{214}Nd at $z \geqslant 8$ fm are less than ^{194}Nd, as shown in Fig. 13(b). However, their slopes of the density are still the smallest. As discussed in Ref. [122], a reduction of the diffuseness along the main axis of deformation develops simultaneously with an increase of the diffuseness along the other axis. Therefore, the oblate deformed ^{204}Nd and ^{214}Nd are the most diffuse ones along the symmetry axis. In Fig. 13(c), since the deformation for $^{124,134,...,194}$Nd is either spherical or prolate, its density distribution perpendicular to the symmetry axis is equal to or smaller than that along the symmetry axis. The densities for oblate ^{204}Nd and ^{214}Nd are much more elongated perpendicular to the symmetry axis and lead to significantly larger density distributions along $r_\perp$.

G. Single-neutron levels in canonical basis

The canonical basis is obtained by diagonalizing the density matrix, with the eigenvalues corresponding to the occupation probabilities [cf. Eq. (25)]. The single-particle energies in the canonical basis are the diagonal matrix elements of the single-particle Hamiltonian in the canonical basis. The canonical basis is very useful to discuss the physics in exotic nuclei [68,70,81,82,93,123].

The single-neutron spectrum around the neutron Fermi energy λ_n in the canonical basis for ^{214}Nd is shown in Fig. 14. As the projection of the angular momentum on the symmetry axis m and the parity π are good quantum numbers in the axially deformed system with spatial reflection symmetry,
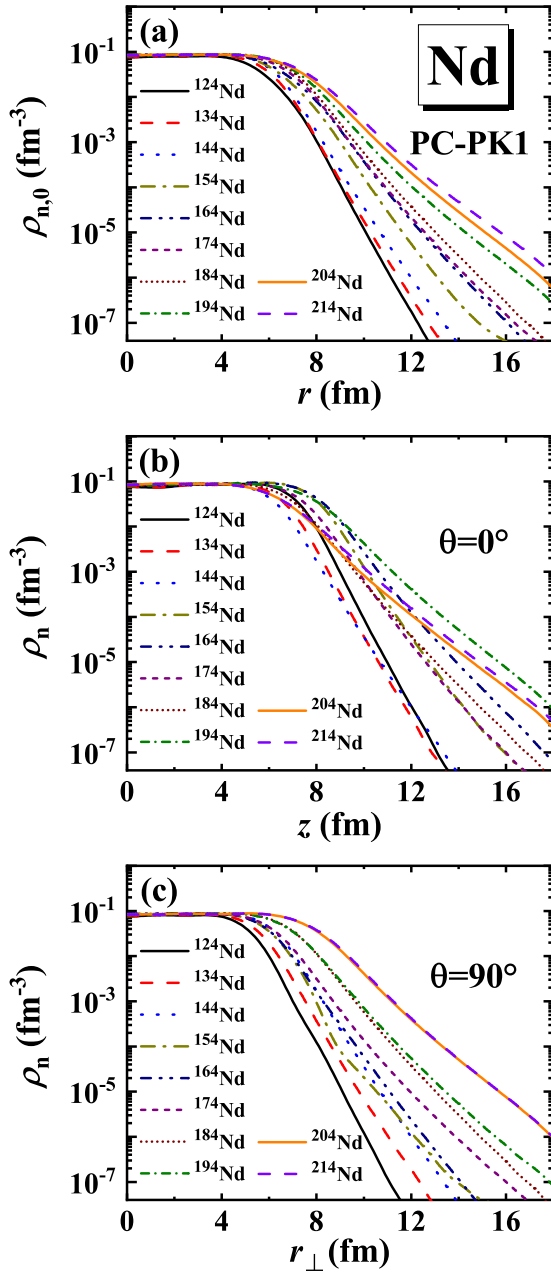
FIG. 13. (a) Spherical component of the neutron density distribution, (b) the neutron density distribution along the symmetry axis z, and (c) the neutron density distribution perpendicular to the symmetry axis with $r_\perp = \sqrt{x^2 + y^2}$, for selected even-even neodymium isotopes $^{124,134,...,214}$Nd in the DRHBc calculations.

FIG. 14. Single-neutron levels around the Fermi energy in the canonical basis for ^{214}Nd versus the occupation probability v^2 in the DRHBc calculations. Each level is labeled by the quantum numbers m^π. The main components and rms radii for the levels with $\epsilon > -0.3$ MeV are also given. The neutron Fermi energy λ_n is shown with the dotted line. The occupation probability from the BCS formula with the average pairing gap is given by the dashed line. The thin solid line represents the continuum threshold.

each state is labeled with m^π. The main components in the spherical Woods-Saxon basis and rms radii for the states with single-neutron energies higher than -0.3 MeV are also given. The lengths of horizontal lines represent the occupation probabilities v^2 in Fig. 14. The occupation probabilities calculated by the BCS formula [89] with the average pairing gap and single-neutron energies in the canonical basis are shown by the dashed line. The bound single-neutron levels are occupied with considerable probabilities, and those with single-neutron energies smaller than -1 MeV are almost fully
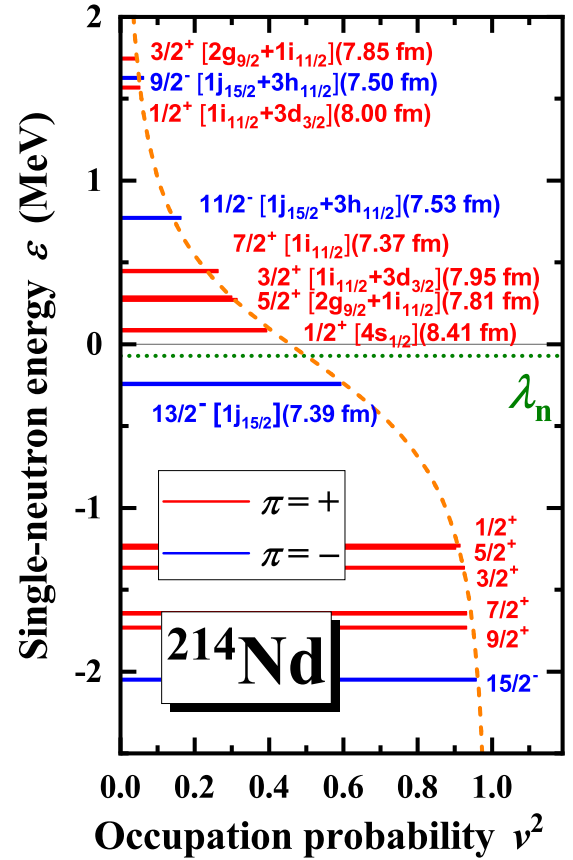
occupied. As the neutron Fermi energy $\lambda_n = -0.07$ MeV and is close to the threshold, the states in the continuum have noticeable occupation probabilities due to the pairing correlation. Since the neutron Fermi energy is negative, the single-neutron densities in the continuum are localized [93] and the nucleus is still bound. The occupation probabilities of both bound states and continuum states are roughly consistent with those calculated by the BCS formula. By summing the number of neutrons in the continuum, one obtains about four neutrons in the continuum, which could be related to the possible neutron halo phenomenon [68,70–72,81,82,124]. The states whose main components are s waves or d waves with low centrifugal barriers have relatively larger rms radii, and are helpful in the formation of halos. It can also be seen in Fig. 13 that ^{214}Nd has significant density distributions in the region of large r, which could be an indicator of exotic structure such as the existence of the neutron halo. This could be also an interesting topic worth further studying, and the strategy in Refs. [81,82] can be employed to investigate such an exotic structure.
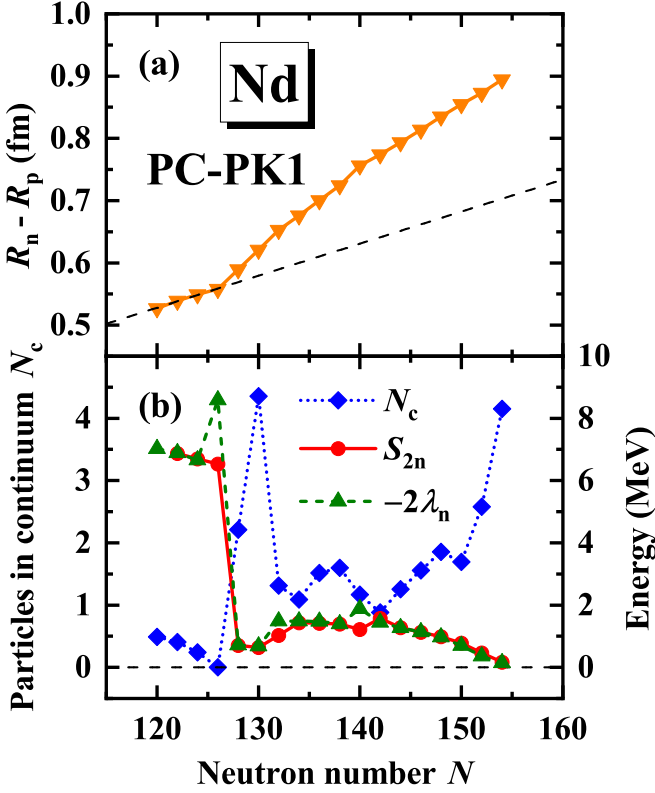
FIG. 15. (a) Thickness of the neutron skin $R_n - R_p$ together with its increasing trend for $N \leqslant 126$ as a dashed line, and (b) the number of particles in the continuum N_c, two-neutron separation energy S_{2n}, and two times the negative neutron Fermi energy, $-2\lambda_n$, as functions of the neutron number for neutron-rich neodymium isotopes with $N \geqslant 120$ in the DRHBc calculations.

H. Neutron skin and proton radioactivity

In order to explore the possible exotic structures in Nd isotopes, the thickness of the neutron skin, the number of particles in the continuum, contributions of different states to the total density, and the proton radioactivity are investigated and discussed in detail.

Figure 15(a) shows the thickness of the neutron skin $R_n - R_p$ for Nd isotopes with $N \geqslant 120$. The thickness of the neutron skin increases gradually from $N = 120$ to $N = 126$ and significantly after the neutron shell closure $N = 126$, and reaches the maximum at the neutron drip-line nucleus ^{214}Nd.

In Fig. 15(b), the number of particles in the continuum N_c, the two-neutron separation energy S_{2n}, and two times the negative neutron Fermi energy, $-2\lambda_n$, for Nd isotopes with $N \geqslant 120$ are shown. The number of particles in the continuum is the sum of occupation probabilities over positive-energy states in the canonical basis. The relation $S_{2n} \approx -2\lambda_n$ is reproduced except for ^{186}Nd due to the pairing collapse and ^{192,200}Nd due to the change of deformation (configuration). For the nuclei with $N > 126$, the neutron Fermi energy is close to the continuum threshold ($\lambda_n > -1$ MeV); as a result neutrons can be scattered into the continuum due to the pairing correlation [69,93]. The sudden increase of N_c and the sudden decrease of S_{2n} after $N = 126$ in Fig. 15(b) coincide with
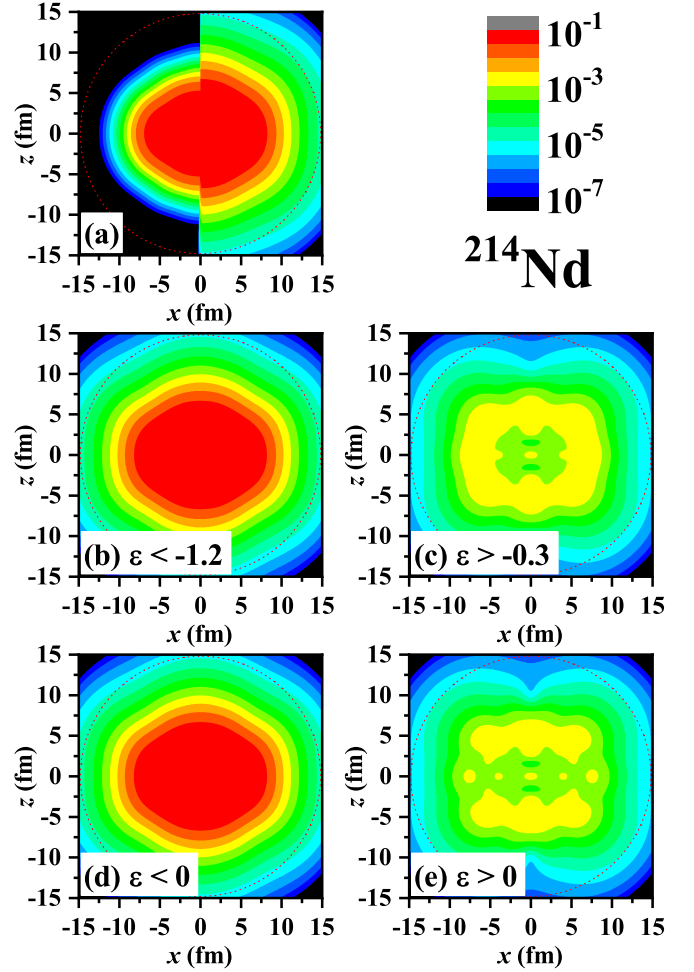

FIG. 16. Density distributions with z axis as the symmetry axis in ^{214}Nd for (a) the proton (for $x < 0$) and the neutron (for $x > 0$), and the neutron with single-particle energy (b) $\epsilon < -1.2$ MeV, (c) $\epsilon > -0.3$ MeV, (d) $\epsilon < 0$ MeV, and (e) $\epsilon > 0$ MeV in the canonical basis. In each plot, a dotted circle is drawn to guide the eye.

the abrupt change in the thickness of neutron skin $R_n - R_p$ in Fig. 15(a). The nuclei with more than two neutrons in the continuum, ^{188}Nd, ^{190}Nd, ^{212}Nd, and ^{214}Nd, have the smallest two-neutron separation energies.

Since for ^{214}Nd, there are more than four neutrons in the continuum, the two-neutron separation energy is less than 0.1 MeV, and the thickness of the neutron skin $R_n - R_p$ is around 0.9 fm, it is encouraging to investigate its density distribution to explore the existence of a possible neutron skin or neutron halo.

In Fig. 16(a), the neutron and proton density distributions for ^{214}Nd are shown. Both the neutron and proton density distributions show oblate shapes, consistent with Fig. 11. Owing to the large neutron excess, the neutron density extends much farther than the proton.

According to the single-particle levels in Fig. 14, there is a gap between the levels with $\epsilon < -1.2$ MeV and those with $\epsilon > -0.3$ MeV. Following the strategy in Refs. [81,82], the neutron density is decomposed into two parts, as shown in Figs. 16(b) for $\epsilon < -1.2$ MeV and 16(c) for $\epsilon > -0.3$ MeV.

The quadrupole deformations are respectively $\beta_2 = -0.268$ for in Fig. 16(b) and $\beta_2 = -0.160$ for $\epsilon > -0.3$ MeV in Fig. 16(c). While both are oblate, they are still slightly decoupled. Although the density in Fig. 16(c) is contributed by the weakly bound states and continuum, it is less diffuse than that in Fig. 16(b) both along and perpendicular to the symmetry axis.

Similarly, the neutron density can be decomposed into the part for bound states with $\epsilon < 0$ MeV in Fig. 16(d) and the part for the continuum with $\epsilon > 0$ MeV in Fig. 16(e). The difference between such a decomposition and the previous one is the allocation of the weakly bound state $13/2^-$, which corresponds to an oblate shape and the main component $1j_{15/2}$ with a mixing of $|Y_{76}(\theta, \varphi)|^2$ and $|Y_{77}(\theta, \varphi)|^2$. This allocation hardly influences the density distribution in Fig. 16(b) and the quadrupole deformation changes slightly to $\beta_2 = -0.273$ in Fig. 16(d). In contrast, the density distribution changes from oblate with $\beta_2 = -0.160$ in Fig. 16(c) to nearly spherical with $\beta_2 = 0.047$ in Fig. 16(e). The decoupling between the oblate shape contributed by bound states and the nearly spherical one by the continuum is remarkable. By comparing Figs. 16(b) and 16(c) or 16(d) and 16(e), there is no clear clue for a halo structure in ^{214}Nd.

Although the theoretical description of light halo nuclei is well under control, as discussed in Refs. [40,125,126], existing definitions and tools are often too qualitative and the associated observables are incomplete for heavier ones. There has been much effort put into quantifying halos by examining the separation energy, the density profiles, the particles in the classically forbidden region, and weakly bound particles obtained from mean field calculations [73,125,127,128]. In this paper, the total neutron density for ^{214}Nd is decomposed into the contributions of different states to examine quantitatively whether the density in the region of large r is mainly contributed by the narrow bunch of weakly bound and positive-energy states to distinguish its halo character.

In order to further identify the nature of neutron halo or neutron skin in ^{214}Nd, the contribution of each single-particle state in the canonical basis to the total neutron density is shown in Fig. 17. Along the symmetry axis, the state $1/2^-$ with $\epsilon = -2.69$ MeV plays the dominant role for large r as shown in Fig. 17(a). Another $1/2^-$ state with $\epsilon = -4.06$ MeV also makes distinguishable contributions for large r. The contribution of the $1/2^+$ state embedded in the continuum becomes more and more important for $r \gtrsim 14$ fm because its main component s wave is free from the centrifugal barrier. Perpendicular to the symmetry axis, several bound states with $\epsilon < -2.6$ MeV together with the $1/2^+$ state in the continuum contribute to the total neutron density for large r as shown in Fig. 17(b). The contribution of the $1/2^+$ state in the continuum evolves similarly at both $\theta = 0°$ and $90°$ due to its nearly spherical density distribution. From Figs. 17(a) and 17(b), it can be clearly seen that the density in the region of large r is mainly contributed by the deeply bound low-m states with $\epsilon < -2.6$ MeV, and the contributions of continuum states except for the $1/2^+$ state are very small because of their high centrifugal barriers as shown in Fig. 14, explaining why the density distributions in Figs. 16(b) and 16(d) are more
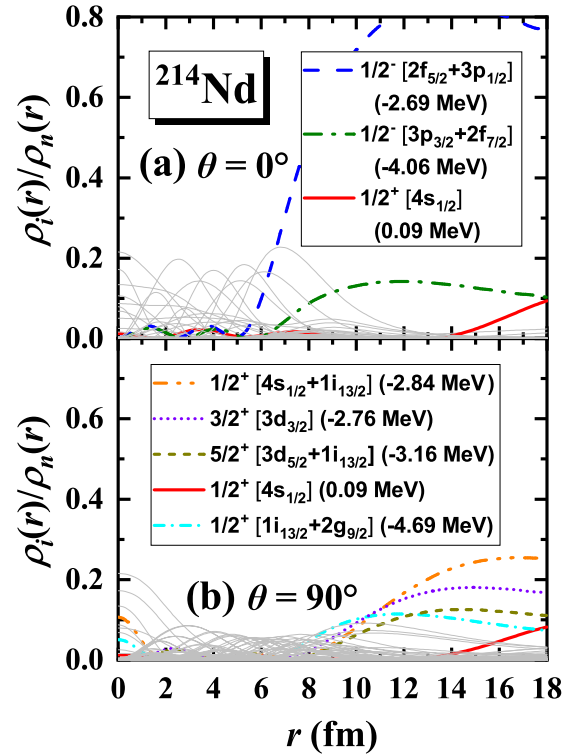

FIG. 17. Contribution of each single-particle state in the canonical basis to the total neutron density at (a) $\theta = 0°$ (along the symmetry axis) and (b) $\theta = 90°$ (perpendicular to the symmetry axis) in ^{214}Nd as a function of the radius. The states with significant contributions ($\gtrsim 0.1$) in the asymptotic area are highlighted and their energies and main components are given.

diffuse than those in Figs. 16(c) and 16(e). Therefore, the halo character in ^{214}Nd can be excluded.

On the proton-rich side, possible exotic phenomena include the proton halo and the proton radioactivity. The interest in the proton radioactivity has been boosted significantly by the discoveries of one- and two-proton emission beyond the proton drip lines [129,130]. Comprehensive theoretical efforts have been made to investigate proton radioactivity based on the CDFT [79,131–134]. Because of its self-consistent treatment of deformation, pairing correlation, and the continuum, it is natural to apply the DRHBc theory to study the proton radioactivity to understand the physics beyond the drip line.

As shown in Fig. 10(b), the proton drip-line nucleus for Nd isotopes in the DRHBc theory is ^{120}Nd. The proton Fermi energies for ^{118}Nd and other lighter even-even Nd isotopes are positive, and they might be unstable against proton emission. However, due to the existence of the Coulomb barrier, some of them may become quasibound proton emitters with certain half-lives. To explore such exotic phenomena, the single-proton spectrum around the proton Fermi energy λ_p in the canonical basis for ^{114}Nd is shown in Fig. 18 as an example. The heights of the Coulomb barrier along and perpendicular to the symmetry axis are given. ^{114}Nd is prolate deformed with $\beta_2 = 0.248$ and $\beta_{p,2} = 0.269$. Accordingly, the height of the Coulomb barrier at $\theta = 0°$ is 9.12 MeV and at $\theta = 90°$ is 10.05 MeV. For ^{114}Nd, the proton Fermi energy
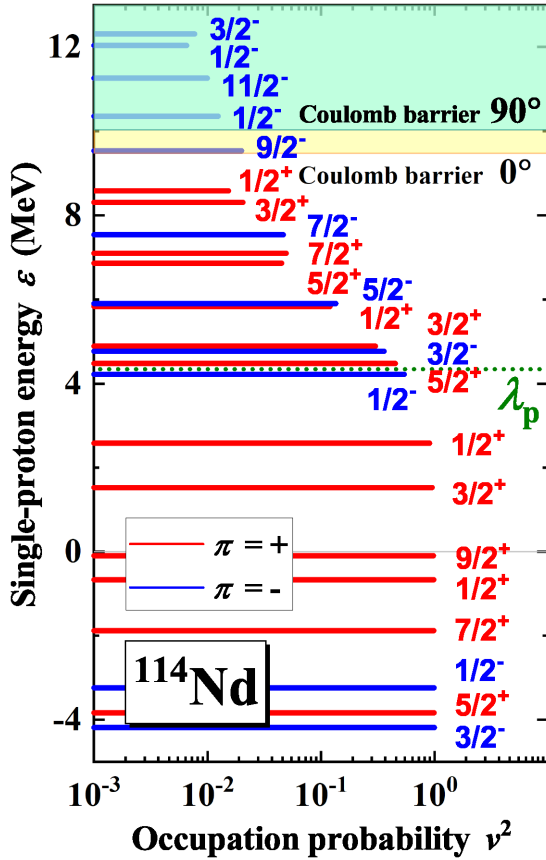
FIG. 18. Single-proton levels around the Fermi energy in the canonical basis for ^{114}Nd versus the occupation probability v^2. Each level is labeled by the quantum numbers m^π. The Fermi energy λ_p is shown as a dotted line. The continuum threshold is represented by a thin solid line. The shaded areas represent respectively the regions above the Coulomb barrier at $0°$ (along the symmetry axis) and $90°$ (perpendicular to the symmetry axis).

$\lambda_p = 4.35$ MeV is below the Coulomb barrier at either $\theta = 0°$ or $90°$. Therefore the protons (≈ 8) above the continuum threshold are still quasibound by the Coulomb barrier. These protons may undergo quantum tunneling. By comparing the calculated binding energies of ^{114}Nd and its two-proton emission daughter nucleus ^{112}Ce, one can find the decay energy $Q_{2p} = -S_{2p} = 8.53$ MeV is positive and thus the two-proton radioactivity is energetically allowed. Similarly, the decay energies $Q_{4p} = 14.95$ MeV, $Q_{6p} = 19.03$ MeV, and $Q_{8p} = 21.17$ MeV for ^{114}Nd are obtained by comparing its binding energy with those of its corresponding daughter nuclei, which suggests the possibility of multiproton radioactivity in ^{114}Nd. Further calculations indicate that ^{116}Nd and ^{118}Nd are also candidates for two-proton and even multiproton radioactivity. Systematical investigation of the proton radioactivity including not only even-even nuclei but also odd-mass nuclei and odd-odd nuclei as well as the decay half-lives is needed.

V. SUMMARY

In summary, the DRHBc theory based on the point-coupling density functionals including both the deformation

and continuum effects is developed. Numerical details towards constructing the DRHBc mass table have been examined. The DRHBc calculation, previously accessible only for light nuclei up to magnesium isotopes, has been extended for all even-even nuclei in the nuclear chart. Taking even-even neodymium isotopes from the proton drip line to the neutron drip line as examples, the ground-state properties and exotic structures are investigated.

The numerical details towards constructing the DRHBc mass table for even-even nuclei with satisfactory accuracy have been examined. For the Dirac Woods-Saxon basis, the box size $R_{box} = 20$ fm, the mesh size $\Delta r = 0.1$ fm, the energy cutoff $E_{cut}^+ = 300$ MeV, and the angular momentum cutoff $J_{max} = 23/2\hbar$ are recommended. For the pairing channel, the pairing strength $V_0 = -325.0$ MeV fm^3 and the pairing window of 100 MeV are suggested. For the Legendre expansion of deformed densities and potentials, the expansion truncation $\lambda_{max} = 6$ is suggested for $Z \leqslant 80$, and $\lambda_{max} = 8$ is suggested for $Z > 80$.

Taking even-even neodymium isotopes from the neutron drip line to the proton drip line as examples, the DRHBc calculations with the density functional PC-PK1 are systematically performed. The strategy to locate the ground states is suggested and confirmed by constrained calculations. The ground-state properties for even-even neodymium isotopes thus obtained are compared with available data and the results in the spherical RCHB mass table [12].

The experimental binding energies for even-even neodymium isotopes are reproduced by the DRHBc calculations with a rms deviation of 0.958 MeV with the rotational correction and 2.668 MeV without the rotational correction, in comparison with 8.301 MeV given by the spherical RCHB calculations. Accordingly, the two-neutron separation energies are better reproduced. The predicted proton and neutron drip-line nuclei are respectively ^{120}Nd and ^{214}Nd, in contrast with ^{126}Nd and ^{228}Nd in the RCHB theory.

The shapes and sizes for even-even neodymium isotopes are correctly reproduced by the DRHBc calculations. Good agreements with the observed quadrupole deformation and its evolution as well as the charge radius and its kink around the shell closure $N = 82$ are obtained.

The neutron density distributions for neodymium isotopic chain are examined. It is found that their spherical components increase with the mass number monotonically. The density of a prolate deformed nucleus is more elongated along the symmetry axis, and an oblate deformed one is more elongated perpendicular to the symmetry axis.

For the most neutron-rich neodymium isotope ^{214}Nd, its two-neutron separation energy is smaller than 0.1 MeV, its neutron skin thickness is around 0.9 fm, and there are more than four neutrons in continuum. By decomposing the neutron density of ^{214}Nd, an interesting decoupling between the oblate shape $\beta_2 = -0.273$ contributed by bound states and the nearly spherical one $\beta_2 = 0.047$ contributed by continuum is found. Contributions of different single-particle states to the total neutron density show that the neutron density in the region of large r is mainly contributed by the deeply bound low-m states with $\epsilon < -2.6$ MeV. Therefore, the exotic character in ^{214}Nd is concluded to be neutron skin instead of halo.

TABLE I. Ground-state properties of Nd isotopes calculated by the DRHBc theory, in comparison with the available data of masses and charge radii. In addition, the data labeled with underline mean the nucleus is unbound.

A	N	$E_b^{Cal.}$ (MeV)	$E_b^{Exp.}$ (MeV)	S_{2n} (MeV)	$E_{rot.}$ (MeV)	R_n (fm)	R_p (fm)	R_m (fm)	$R_C^{Cal.}$ (fm)	$R_C^{Exp.}$ (fm)	$\beta_{n,2}$	$\beta_{p,2}$	β_2	λ_n (MeV)	λ_p (MeV)
$Z = 60$ (Nd)
118	58	914.566			2.534	4.707	4.826	4.768	4.892		0.395	0.427	0.411	−15.622	<u>0.752</u>
120	60	945.402		30.837	2.424	4.745	4.833	4.789	4.899		0.411	0.433	0.422	−15.915	−0.320
122	62	971.808		26.406	2.664	4.784	4.842	4.812	4.907		0.418	0.431	0.425	−12.925	−0.804
124	64	996.962		25.154	2.510	4.813	4.848	4.830	4.913		0.404	0.418	0.411	−12.409	−1.552
126	66	1021.140		24.178	2.398	4.841	4.854	4.847	4.919		0.389	0.405	0.396	−11.836	−1.051
128	68	1043.878		22.739	2.571	4.874	4.863	4.869	4.928		0.375	0.391	0.383	−11.182	−1.718
130	70	1065.647	1068.93	21.768	2.789	4.942	4.906	4.926	4.971		0.429	0.437	0.433	−10.801	−2.361
132	72	1086.839	1089.90	21.192	2.750	4.991	4.935	4.965	4.999	4.917	0.451	0.459	0.455	−11.057	−3.034
134	74	1106.479	1110.26	19.640	2.464	4.923	4.845	4.888	4.911	4.911	0.218	0.233	0.224	−10.210	−3.275
136	76	1126.347	1129.96	19.869	2.466	4.945	4.846	4.902	4.911	4.911	0.174	0.193	0.182	−9.918	−3.769
138	78	1145.921	1148.92	19.574	2.250	4.968	4.847	4.916	4.913	4.912	0.126	0.148	0.136	−9.867	−4.320
140	80	1165.771	1167.30	19.850	0.000	4.988	4.846	4.928	4.912	4.910	0.000	0.000	0.000	−10.367	−4.957
142	82	1186.396	1185.14	20.625	0.000	5.014	4.854	4.947	4.920	4.912	0.000	0.000	0.000	−11.276	−5.564
144	84	1197.425	1199.08	11.029	0.000	5.060	4.879	4.985	4.944	4.942	0.000	0.000	0.000	−5.586	−6.181
146	86	1209.470	1212.40	12.044	1.858	5.116	4.915	5.034	4.979	4.970	0.152	0.157	0.154	−6.464	−6.880
148	88	1222.446	1225.02	12.976	1.795	5.167	4.949	5.080	5.013	5.000	0.210	0.218	0.213	−6.357	−7.536
150	90	1235.217	1237.44	12.771	2.306	5.264	5.034	5.173	5.098	5.040	0.365	0.380	0.371	−6.791	−8.666
152	92	1248.387	1250.05	13.170	2.136	5.289	5.046	5.194	5.109		0.353	0.370	0.360	−6.040	−9.198
154	94	1259.341	1261.73	10.954	2.333	5.329	5.063	5.227	5.126		0.362	0.374	0.367	−5.440	−11.073
156	96	1269.848	1272.66	10.507	2.318	5.368	5.083	5.260	5.145		0.371	0.377	0.373	−5.227	−11.636
158	98	1280.006		10.158	2.173	5.406	5.102	5.293	5.164		0.379	0.380	0.379	−5.027	−12.190
160	100	1289.755		9.750	0.000	5.445	5.120	5.325	5.182		0.385	0.381	0.383	−5.321	−11.700
162	102	1297.790		8.034	2.329	5.493	5.145	5.367	5.207		0.404	0.393	0.400	−3.976	−12.153
164	104	1305.500		7.710	2.420	5.551	5.178	5.417	5.240		0.441	0.418	0.433	−3.771	−12.553
166	106	1312.218		6.718	2.459	5.534	5.150	5.398	5.211		0.332	0.325	0.329	−3.686	−12.993
168	108	1319.405		7.186	2.353	5.562	5.156	5.420	5.218		0.305	0.297	0.302	−3.623	−13.316
170	110	1326.380		6.975	2.248	5.593	5.166	5.446	5.227		0.288	0.280	0.285	−3.405	−13.639
172	112	1332.717		6.337	2.363	5.619	5.174	5.468	5.235		0.264	0.260	0.262	−3.102	−13.944
174	114	1338.609		5.892	2.337	5.641	5.177	5.486	5.239		0.226	0.231	0.228	−3.036	−14.169
176	116	1344.536		5.927	2.185	5.663	5.180	5.503	5.242		0.178	0.190	0.182	−3.169	−14.390
178	118	1350.839		6.303	2.006	5.687	5.179	5.521	5.240		0.108	0.119	0.112	−3.431	−14.672
180	120	1357.637		6.798	0.000	5.713	5.186	5.543	5.247		0.041	0.046	0.043	−3.509	−14.925
182	122	1364.528		6.891	0.000	5.739	5.200	5.567	5.261		0.000	0.000	0.000	−3.442	−15.282
184	124	1371.289		6.761	0.000	5.765	5.216	5.592	5.277		0.000	0.000	0.000	−3.327	−15.689
186	126	1377.904		6.615	0.000	5.790	5.232	5.616	5.293		0.000	0.000	0.000	−4.294	−16.104
188	128	1378.449		0.545	0.000	5.835	5.246	5.654	5.306		0.000	0.000	0.000	−0.357	−16.377
190	130	1378.950		0.510	0.000	5.880	5.259	5.691	5.320		0.000	0.000	0.000	−0.339	−16.650
192	132	1379.474		0.524	1.318	5.937	5.284	5.740	5.344		0.141	0.100	0.128	−0.744	−17.208
194	134	1381.344		1.870	1.423	5.981	5.305	5.781	5.365		0.174	0.129	0.160	−0.740	−17.564
196	136	1382.679		1.335	1.540	6.026	5.325	5.820	5.385		0.200	0.153	0.186	−0.738	−17.835
198	138	1384.006		1.327	1.562	6.070	5.345	5.860	5.405		0.222	0.175	0.208	−0.698	−18.072
200	140	1385.306		1.300	1.802	6.144	5.388	5.928	5.447		−0.255	−0.238	−0.250	−0.940	−18.574
202	142	1386.801		1.495	1.928	6.180	5.406	5.961	5.465		−0.260	−0.242	−0.255	−0.720	−18.871
204	144	1387.977		1.176	2.014	6.216	5.422	5.993	5.481		−0.263	−0.242	−0.257	−0.632	−19.141
206	146	1389.044		1.066	2.008	6.251	5.437	6.025	5.496		−0.266	−0.242	−0.259	−0.567	−19.405
208	148	1389.992		0.948	1.919	6.287	5.452	6.058	5.510		−0.269	−0.242	−0.261	−0.485	−19.667
210	150	1390.745		0.753	1.803	6.322	5.468	6.090	5.526		−0.271	−0.243	−0.263	−0.350	−19.935
212	152	1391.163		0.418	1.795	6.357	5.484	6.122	5.542		−0.271	−0.243	−0.263	−0.178	−20.204
214	154	1391.261		0.097	1.870	6.390	5.495	6.152	5.553		−0.264	−0.237	−0.257	−0.071	−20.428
216	156	1391.204		<u>−0.057</u>	1.889	6.421	5.503	6.179	5.561		−0.252	−0.225	−0.244	−0.025	−20.623

For the proton-rich side, by examining the proton single-particle energies, the Fermi energy, and the Coulomb barrier for ^{114}Nd beyond the proton drip line, possible two-proton and even multiproton emissions are predicted. Further calculations show that ^{116}Nd and ^{118}Nd are also candidates for two-proton and even multiproton radioactivity. Future investigation of the proton radioactivity including not only even-even nuclei but also odd-mass nuclei and odd-odd nuclei as well as the decay half-lives is needed.

ACKNOWLEDGMENTS

APPENDIX: TABULATION OF GROUND-STATE PROPERTIES

The ground-state properties of even-even Nd isotopes are tabulated in Table I.

[1] J. Meng, *Relativistic Density Functional for Nuclear Structure* (World Scientific, Singapore, 2016).

[2] W. Zhan, H. Xu, G. Xiao, J. Xia, H. Zhao, and Y. Yuan, Nucl. Phys. A **834**, 694c (2010).

[3] T. Motobayashi, Nucl. Phys. A **834**, 707c (2010).

[4] K. Tshoo, Y. Kim, Y. Kwon, H. Woo, G. Kim, Y. Kim, B. Kang, S. Park, Y.-H. Park, J. Yoon *et al.*, Nucl. Instrum. Methods Phys. Res. A **317**, 242 (2013).

[5] C. Sturm, B. Sharkov, and H. Stcker, Nucl. Phys. A **834**, 682c (2010).

[6] S. Gales, Nucl. Phys. A **834**, 717c (2010).

[7] M. Thoennessen, Nucl. Phys. A **834**, 688c (2010).

[8] D. Lunney, J. Pearson, and C. Thibault, Rev. Mod. Phys. **75**, 1021 (2003).

[9] K. Blaum, Phys. Rep. **425**, 1 (2006).

[10] J. Erler, N. Birge, M. Kortelainen, W. Nazarewicz, E. Olsen, A. M. Perhac, and M. Stoitsov, Nature (London) **486**, 509 (2012).

[11] M. Thoennessen, Rep. Prog. Phys. **76**, 056301 (2013).

[12] X. W. Xia, Y. Lim, P. W. Zhao, H. Z. Liang, X. Y. Qu, Y. Chen, H. Liu, L. F. Zhang, S. Q. Zhang, Y. Kim *et al.*, At. Data Nucl. Data Tables **121–122**, 1 (2018).

[13] National Nuclear Data Center (NNDC), http://www.nndc.bnl.gov/.

[14] W. J. Huang, G. Audi, M. Wang, F. G. Kondev, S. Naimi, and X. Xu, Chin. Phys. C **41**, 030002 (2017).

[15] M. Wang, G. Audi, F. G. Kondev, W. J. Huang, S. Naimi, and X. Xu, Chin. Phys. C **41**, 030003 (2017).

[16] Z. Y. Zhang, Z. G. Gan, H. B. Yang, L. Ma, M. H. Huang, C. L. Yang, M. M. Zhang, Y. L. Tian, Y. S. Wang, M. D. Sun *et al.*, Phys. Rev. Lett. **122**, 192503 (2019).

[17] P. Möller, A. Sierk, T. Ichikawa, and H. Sagawa, At. Data Nucl. Data Tables **109–110**, 1 (2016).

[18] Y. Aboussir, J. Pearson, A. Dutta, and F. Tondeur, At. Data Nucl. Data Tables **61**, 127 (1995).

[19] N. Wang, M. Liu, X. Wu, and J. Meng, Phys. Lett. B **734**, 215 (2014).

[20] H. Zhang, J. Dong, N. Ma, G. Royer, J. Li, and H. Zhang, Nucl. Phys. A **929**, 38 (2014).

[21] M. Samyn, S. Goriely, P.-H. Heenen, J. Pearson, and F. Tondeur, Nucl. Phys. A **700**, 142 (2002).

[22] M. V. Stoitsov, J. Dobaczewski, W. Nazarewicz, S. Pittel, and D. J. Dean, Phys. Rev. C **68**, 054312 (2003).

[23] S. Goriely, N. Chamel, and J. M. Pearson, Phys. Rev. Lett. **102**, 152503 (2009).

[24] S. Goriely, N. Chamel, and J. M. Pearson, Phys. Rev. C **88**, 024308 (2013).

[25] S. Hilaire and M. Girod, Eur. Phys. J. A **33**, 237 (2007).

[26] S. Goriely, S. Hilaire, M. Girod, and S. Péru, Phys. Rev. Lett. **102**, 242501 (2009).

[27] J. P. Delaroche, M. Girod, J. Libert, H. Goutte, S. Hilaire, S. Péru, N. Pillet, and G. F. Bertsch, Phys. Rev. C **81**, 014303 (2010).

[28] G. Lalazissis, S. Raman, and P. Ring, At. Data Nucl. Data Tables **71**, 1 (1999).

[29] L.-S. Geng, H. Toki, and J. Meng, Prog. Theor. Phys. **113**, 785 (2005).

[30] J. Meng, J. Peng, S. Q. Zhang, and P. W. Zhao, Front. Phys. **8**, 55 (2013).

[31] Q. S. Zhang, Z. M. Niu, Z. P. Li, J. M. Yao, and J. Meng, Front. Phys. **9**, 529 (2014).

[32] S. E. Agbemava, A. V. Afanasjev, D. Ray, and P. Ring, Phys. Rev. C **89**, 054320 (2014).

[33] A. V. Afanasjev, S. E. Agbemava, D. Ray, and P. Ring, Phys. Rev. C **91**, 014324 (2015).

[34] K. Q. Lu, Z. X. Li, Z. P. Li, J. M. Yao, and J. Meng, Phys. Rev. C **91**, 027304 (2015).

[35] D. Peña-Arteaga, S. Goriely, and N. Chamel, Eur. Phys. J. A **52**, 320 (2016).

[36] P. Ring, Prog. Part. Nucl. Phys. **37**, 193 (1996).

[37] D. Vretenar, A. V. Afanasjev, G. A. Lalazissis, and P. Ring, Phys. Rep. **409**, 101 (2005).

[38] J. Meng, H. Toki, S. G. Zhou, S. Q. Zhang, W. H. Long, and L. S. Geng, Prog. Part. Nucl. Phys. **57**, 470 (2006).

[39] T. Niksic, D. Vretenar, and P. Ring, Prog. Part. Nucl. Phys. **66**, 519 (2011).

[40] J. Meng and S. G. Zhou, J. Phys. G **42**, 093101 (2015).

[41] S.-G. Zhou, Phys. Scr. **91**, 063008 (2016).

[42] S. Shen, H. Liang, W. H. Long, J. Meng, and P. Ring, Prog. Part. Nucl. Phys. **109**, 103713 (2019).

[43] J. N. Ginocchio, Phys. Rev. Lett. **78**, 436 (1997).

[44] J. Meng, K. Sugawara-Tanabe, S. Yamaji, P. Ring, and A. Arima, Phys. Rev. C **58**, R628(R) (1998).

[45] J. Meng, K. Sugawara-Tanabe, S. Yamaji, and A. Arima, Phys. Rev. C **59**, 154 (1999).

[46] T. S. Chen, H. F. Lu, J. Meng, S. Q. Zhang, and S. G. Zhou, Chin. Phys. Lett. **20**, 358 (2003).

[47] J. N. Ginocchio, Phys. Rep. **414**, 165 (2005).

[48] H. Liang, J. Meng, and S.-G. Zhou, Phys. Rep. **570**, 1 (2015).

[49] S.-G. Zhou, J. Meng, and P. Ring, Phys. Rev. Lett. **91**, 262501 (2003).

[50] X. T. He, S. G. Zhou, J. Meng, E. G. Zhao, and W. Scheid, Eur. Phys. J. A **28**, 265 (2006).

[51] W. Koepf and P. Ring, Nucl. Phys. A **493**, 61 (1989).

[52] J. M. Yao, H. Chen, and J. Meng, Phys. Rev. C **74**, 024307 (2006).

[53] A. Arima, Sci. China Phys. Mech. Astron. **54**, 188 (2011).

[54] J. Li, J. Meng, P. Ring, J. M. Yao, and A. Arima, Sci. China Phys. Mech. Astron. **54**, 204 (2011).

[55] J. Li, J. M. Yao, J. Meng, and A. Arima, Prog. Theor. Phys. **125**, 1185 (2011).

[56] J. Li and J. Meng, Front. Phys. **13**, 132109 (2018).

[57] J. König and P. Ring, Phys. Rev. Lett. **71**, 3079 (1993).

[58] A. V. Afanasjev, P. Ring, and J. Konig, Nucl. Phys. A **676**, 196 (2000).

[59] A. V. Afanasjev and P. Ring, Phys. Rev. C **62**, 031302(R) (2000).

[60] A. V. Afanasjev and H. Abusara, Phys. Rev. C **82**, 034329 (2010).

[61] P. W. Zhao, J. Peng, H. Z. Liang, P. Ring, and J. Meng, Phys. Rev. Lett. **107**, 122501 (2011).

[62] P. W. Zhao, S. Q. Zhang, J. Peng, H. Z. Liang, P. Ring, and J. Meng, Phys. Lett. B **699**, 181 (2011).

[63] P. W. Zhao, J. Peng, H. Z. Liang, P. Ring, and J. Meng, Phys. Rev. C **85**, 054310 (2012).

[64] P. W. Zhao, N. Itagaki, and J. Meng, Phys. Rev. Lett. **115**, 022501 (2015).

[65] Y. K. Wang, Phys. Rev. C **96**, 054324 (2017).

[66] Y. K. Wang, Phys. Rev. C **97**, 064321 (2018).

[67] Z. X. Ren, S. Q. Zhang, P. W. Zhao, N. Itagaki, J. A. Maruhn, and J. Meng, Sci. China Phys. Mech. Astron. **62**, 112062 (2019).

[68] J. Meng and P. Ring, Phys. Rev. Lett. **77**, 3963 (1996).

[69] J. Meng, Nucl. Phys. A **635**, 3 (1998).

[70] J. Meng and P. Ring, Phys. Rev. Lett. **80**, 460 (1998).

[71] J. Meng, H. Toki, J. Y. Zeng, S. Q. Zhang, and S.-G. Zhou, Phys. Rev. C **65**, 041302(R) (2002).

[72] S. Q. Zhang, J. Meng, S. G. Zhou, and J. Y. Zeng, Chin. Phys. Lett. **19**, 312 (2002).

[73] J. Meng, I. Tanihata, and S. Yamaji, Phys. Lett. B **419**, 1 (1998).

[74] J. Meng, S. G. Zhou, and I. Tanihata, Phys. Lett. B **532**, 209 (2002).

[75] W. Zhang, J. Meng, S. Q. Zhang, L. S. Geng, and H. Toki, Nucl. Phys. A **753**, 106 (2005).

[76] H. F. Lu, J. Meng, S. Q. Zhang, and S. G. Zhou, Eur. Phys. J. A **17**, 19 (2003).

[77] P. W. Zhao, Z. P. Li, J. M. Yao, and J. Meng, Phys. Rev. C **82**, 054319 (2010).

[78] L.-F. Zhang and X.-W. Xia, Chin. Phys. C **40**, 054102 (2016).

[79] Y. Lim, X. Xia, and Y. Kim, Phys. Rev. C **93**, 014314 (2016).

[80] S.-G. Zhou, J. Meng, S. Yamaji, and S.-C. Yang, Chin. Phys. Lett. **17**, 717 (2000).

[81] S.-G. Zhou, J. Meng, P. Ring, and E.-G. Zhao, Phys. Rev. C **82**, 011301(R) (2010).

[82] L. Li, J. Meng, P. Ring, E.-G. Zhao, and S.-G. Zhou, Phys. Rev. C **85**, 024312 (2012).

[83] S.-G. Zhou, J. Meng, and P. Ring, Phys. Rev. C **68**, 034323 (2003).

[84] Y. Chen, L. Li, H. Liang, and J. Meng, Phys. Rev. C **85**, 067301 (2012).

[85] L. Li, J. Meng, P. Ring, E.-G. Zhao, and S.-G. Zhou, Chin. Phys. Lett. **29**, 042101 (2012).

[86] X.-X. Sun, J. Zhao, and S.-G. Zhou, Phys. Lett. B **785**, 530 (2018).

[87] K. Y. Zhang, D. Y. Wang, and S. Q. Zhang, Phys. Rev. C **100**, 034312 (2019).

[88] W. Koepf and P. Ring, Z. Phys. A **339**, 81 (1991).

[89] P. Ring and P. Schuck, *The Nuclear Many-body Problem* (Springer-Verlag, Berlin, 1980).

[90] B. Pritychenko, M. Birch, B. Singh, and M. Horoi, At. Data Nucl. Data Tables **107**, 1 (2016).

[91] I. Angeli and K. Marinova, At. Data Nucl. Data Tables **99**, 69 (2013).

[92] T. Bürvenich, D. G. Madland, J. A. Maruhn, and P.-G. Reinhard, Phys. Rev. C **65**, 044308 (2002).

[93] J. Dobaczewski, H. Flocard, and J. Treiner, Nucl. Phys. A **422**, 103 (1984).

[94] H. Kucharek and P. Ring, Z. Phys. A **339**, 23 (1991).

[95] T. Gonzalez-Llarena, J. Egido, G. Lalazissis, and P. Ring, Phys. Lett. B **379**, 13 (1996).

[96] M. Serra and P. Ring, Phys. Rev. C **65**, 064324 (2002).

[97] C. E. Price and G. E. Walker, Phys. Rev. C **36**, 354 (1987).

[98] M. Grasso, N. Sandulescu, N. Van Giai, and R. J. Liotta, Phys. Rev. C **64**, 064321 (2001).

[99] N. Michel, K. Matsuyanagi, and M. Stoitsov, Phys. Rev. C **78**, 044319 (2008).

[100] J. C. Pei, A. T. Kruppa, and W. Nazarewicz, Phys. Rev. C **84**, 024311 (2011).

[101] Y. Zhang, M. Matsuo, and J. Meng, Phys. Rev. C **86**, 054318 (2012).

[102] M. Bender, K. Rutz, P.-G. Reinhard, and J. Maruhn, Eur. Phys. J. A **7**, 467 (2000).

[103] W. Long, J. Meng, N. Van Giai, and S.-G. Zhou, Phys. Rev. C **69**, 034319 (2004).

[104] P. W. Zhao, B. Y. Sun, and J. Meng, Chin. Phys. Lett. **26**, 112102 (2009).

[105] P. W. Zhao, L. S. Song, B. Sun, H. Geissel, and J. Meng, Phys. Rev. C **86**, 064324 (2012).

[106] C. Pan, K. Zhang, and S. Zhang, Int. J. Mod. Phys. E **28**, 1950082 (2019).

[107] U. Hofmann and P. Ring, Phys. Lett. B **214**, 307 (1988).

[108] K. Rutz, M. Bender, P.-G. Reinhard, J. Maruhn, and W. Greiner, Nucl. Phys. A **634**, 67 (1998).

[109] K. Rutz, M. Bender, P.-G. Reinhard, and J. Maruhn, Phys. Lett. B **468**, 1 (1999).

[110] J. Meng, J. Peng, S. Q. Zhang, and S.-G. Zhou, Phys. Rev. C **73**, 037303 (2006).

[111] H. F. Lu, L. S. Geng, and J. Meng, Eur. Phys. J. A **31**, 273 (2007).

[112] B.-H. Sun and J. Li, Chin. Phys. C **32**, 882 (2008).

[113] J. Li, J.-M. Yao, and J. Meng, Chin. Phys. C **33**, 98 (2009).

[114] W. Zhang, J. Peng, and S.-Q. Zhang, Chin. Phys. Lett. **26**, 052101 (2009).

[115] A. Staszczak, M. Stoitsov, A. Baran, and W. Nazarewicz, Eur. Phys. J. A **46**, 85 (2010).

[116] Z. P. Li, T. Nikšić, P. Ring, D. Vretenar, J. M. Yao, and J. Meng, Phys. Rev. C **86**, 034334 (2012).

[117] J. Libert, M. Girod, and J.-P. Delaroche, Phys. Rev. C **60**, 054301 (1999).

[118] M. Bender, G. F. Bertsch, and P.-H. Heenen, Phys. Rev. C **73**, 034322 (2006).

[119] M. Bender, G. F. Bertsch, and P.-H. Heenen, Phys. Rev. C **78**, 054312 (2008).

[120] J. Xiang, Z. P. Li, W. H. Long, T. Nikšić, and D. Vretenar, Phys. Rev. C **98**, 054308 (2018).

[121] Z. P. Li, T. Nikšić, D. Vretenar, J. Meng, G. A. Lalazissis, and P. Ring, Phys. Rev. C **79**, 054301 (2009).

[122] G. Scamps, D. Lacroix, G. G. Adamian, and N. V. Antonenko, Phys. Rev. C **88**, 064327 (2013).

[123] J. Dobaczewski, W. Nazarewicz, T. R. Werner, J. F. Berger, C. R. Chinn, and J. Dechargé, Phys. Rev. C **53**, 2809 (1996).

[124] J. Terasaki, S. Q. Zhang, S. G. Zhou, and J. Meng, Phys. Rev. C **74**, 054318 (2006).

[125] V. Rotival and T. Duguet, Phys. Rev. C **79**, 054308 (2009).

[126] V. Rotival, K. Bennaceur, and T. Duguet, Phys. Rev. C **79**, 054309 (2009).

[127] S. Im and J. Meng, Phys. Rev. C **61**, 047302 (2000).

[128] S. Mizutori, J. Dobaczewski, G. A. Lalazissis, W. Nazarewicz, and P.-G. Reinhard, Phys. Rev. C **61**, 044326 (2000).

[129] B. Blank and M. Borge, Prog. Part. Nucl. Phys. **60**, 403 (2008).

[130] M. Pfützner, M. Karny, L. V. Grigorenko, and K. Riisager, Rev. Mod. Phys. **84**, 567 (2012).

[131] D. Vretenar, G. A. Lalazissis, and P. Ring, Phys. Rev. Lett. **82**, 4595 (1999).

[132] J. M. Yao, B. Sun, P. J. Woods, and J. Meng, Phys. Rev. C **77**, 024315 (2008).

[133] L. Ferreira, E. Maglione, and P. Ring, Phys. Lett. B **701**, 508 (2011).

[134] Q. Zhao, J. M. Dong, J. L. Song, and W. H. Long, Phys. Rev. C **90**, 054326 (2014).